Textures of eclogites and blueschists from Syros island, Greece: inferences for elastic anisotropy of subducted oceanic crust

Ruth Keppler (1), Jan H. Behrmann (2), Michael Stipp (3)

(1) Steinmann Institute, Poppelsdorfer Schloss, 53115 Bonn, Germany rkep@uni-bonn.de
(2) Department of Geodynamics, GEOMAR Helmholtz Centre for Ocean Research Kiel, Wischhofstr. 1-3, 24148 Kiel, Germany
(3) Institute of Geology, University of Innsbruck, Innrain 52, A-6020 Innsbruck, Austria

Many blueschists and eclogites are inferred to have formed from oceanic basalts in subducted slabs. Knowledge of their elastic behaviour is essential for reconstructing the internal structure of subduction zones. The Cycladic Blueschist Unit, exposed on Syros Island (Greece), contains rocks belonging to an exhumed Tertiary subduction complex. They were possibly part of a subduction channel, a shear zone above the subducting slab in which exhumation is possible during subduction. Intense plastic deformation, forming crystallographic preferred orientations (CPO), accompanied blueschist and eclogite metamorphism. CPO of the constituent minerals in the collected samples was determined by time-of-flight neutron diffraction. Two samples are foliated fine-grained blueschists with strong CPO, rich in glaucophane, zoisite and phengite. Two coarser-grained eclogite samples rich in omphacite and clinozoisite, or glaucophane, have weaker CPO. Vp and Vs anisotropies were computed from the orientation distribution function and single-crystal elastic constants. All samples show velocity maxima parallel to the mineral lineation, and minima normal to the foliation, providing important constraints on orientations of seismic anisotropy in subduction channels. Vp anisotropies are up to three times higher (6.5-12%) in the blueschists than in the eclogites (3-4%), pointing to a potentially important lithological control of elastic anisotropy in subducted oceanic crust.

Plain Language Summary

Many blueschists and eclogites are inferred to have formed from oceanic basalts in subducted slabs. Knowledge of their elastic behaviour is essential for reconstructing the internal structure of subduction zones. The Cycladic Blueschist Unit, exposed on Syros Island (Greece), contains rocks belonging to an exhumed Tertiary subduction complex. They were possibly part of a subduction channel, a shear zone above the subducting slab in which exhumation is possible during subduction. Intense plastic deformation, forming crystallographic preferred orientations (CPO), accompanied blueschist and eclogite metamorphism. CPO of the constituent minerals in the collected samples was determined by time-of-flight neutron diffraction. Two samples are foliated fine-grained blueschists with strong CPO, rich in glaucophane, zoisite and phengite. Two coarser-grained eclogite samples rich in omphacite and clinozoisite, or glaucophane, have weaker CPO. Vp and Vs anisotropies were computed from the orientation distribution function and single-crystal elastic constants. All samples show velocity maxima parallel to the mineral lineation, and minima normal to the foliation, providing important constraints on orientations of seismic anisotropy in subduction channels. Vp

This article has been accepted for publication and undergone full peer review but has not been through the copyediting, typesetting, pagination and proofreading process which may lead to differences between this version and the Version of Record. Please cite this article as doi: 10.1002/2017JB014181

anisotropies are up to three times higher (6.5-12%) in the blueschists than in the eclogites (3-4%), pointing to a potentially important lithological control of elastic anisotropy in subducted oceanic crust.

1. Introduction

Knowledge of key rock petrophysical properties is essential for reliable interpretation of seismic data. Most important is seismic velocity and its anisotropy, mainly controlled by the rock type, microstructure and the crystallographic preferred orientation (CPO) of the constituent mineral phases (e.g.: Ji. et al., 2003a; b). Despite decades of investigation, subduction zones, especially their acoustic properties at depth, are still a matter of debate (e.g. Helffrich and Stein, 1993; Essen et al. 2009; Audet et al. 2009). As velocity models from active and passive seismic surveys allow for progressively better spatial resolution, knowledge of elastic anisotropy of the constituent rocks becomes increasingly important.

Blueschists and eclogites are the subducted equivalents of basaltic oceanic crust (e.g. Ernst, 1988; Maruyama et al., 1996). Direct links between blueschist occurrence and active subduction have been successfully demonstrated (e.g. Maekawa et al., 1993; Fryer at al., 1999). Thus, the investigation of these rocks and the geometrical, tectonic and petrological reconstructions of fossil subduction complexes (e.g. Wakabayashi, 1999 Wakabayashi et al., 2015, and references therein) offer invaluable insights into fundamental processes of burial, deformation and exhumation as well as into the internal structure of subduction zones and/ or subduction channels (e.g. Behrmann and Ratschbacher 1989; Platt, 1993; Jolivet et al., 2003; Abalos et al., 2003; Malusa et al., 2011, Behr and Platt, 2013).

In seismic images the crust of some subducted oceanic slabs appears as a zone of lower seismic velocities compared to the surrounding mantle of the downgoing and overriding plates (up to 14% velocity difference to up to 150 km depth; e.g. Abers, 2005). This crust is preferentially composed of blueschists and/or eclogites, and is usually seismically anisotropic (e.g. Ji and Zhao, 1994; Ji et al., 1998; Kim et al., 2013). Knowledge of the orientation and magnitude of this anisotropy is, therefore, essential for the correct construction of seismic velocity models and an improved structural interpretation of subducted slabs. One approach is to investigate the anisotropy of rocks by experimental techniques at elevated pressures (e.g. Christensen, 1965; 1966; Christensen and Fountain, 1975; Kern, 1978; 1993; Fountain et al., 1994; Mauler et al., 2000; Ullemeyer et al., 2006; 2010; Kern et al., 2008), or by the recalculation of the elastic velocity using rock texture and single crystal elastic data (e.g. Bascou et al., 2001; Ji et al., 2003; Abalos et al., 2011; Keppler et al., 2015). The major issue we address in this study is how anisotropy is expected to vary between blueschist-grade and eclogite-grade subducted oceanic crust, and how it would compare with the surrounding mantle rocks. This is important, as blueschists and eclogites occupy different fields in pressure-temperature space and, therefore, reflect depth of subduction. Our study object is the Cycladic Blueschist Unit (Aegean Sea, Greece). Especially on the island of Syros high-pressure rocks of oceanic origin are well studied and coherently exposed, including blueschists and eclogites.

2. Geological Setting, Syros Island

The Cycladic Blueschist unit (Fig. 1A,C), arguably one of the best-exposed fossil subduction complexes in the world (e.g., Le Pichon and Angelier, 1979; Gautier et al., 1993; Gautier and Brun, 1994; Ring and Layer, 2003; Ring and Glodny, 2010; Jolivet et al., 2013; Roche et al., 2016), has one of its most extensive occurrences on Syros Island Greece (e.g. Keiter et al., 2004). Former oceanic crust of probable Cretaceous age (Keiter et al., 2011) was subducted within the Mesohellenic Subduction System on a pressure-dominated prograde pressure-temperature path (PT-path; Fig. 1B), and rapidly exhumed thereafter. The Cycladic Blueschist Unit comprises a wide range of blueschists and eclogites with variable fabrics and compositions. The eclogites and especially the blueschists in the areas chosen for sampling (Fig. 1C) are very fresh and known for their low degree of retrogression and overprinting. This offers an ideal background for a systematic study of microstructure, CPO and petrophysical properties of subducted rocks. The metamorphic and structural record allows in principle to decipher processes of burial, high-pressure deformation and exhumation.

The Cycladic Blueschist Unit forms part of the Attic-Cycladic Crystalline Complex, which can be traced from southeast of Euboea island eastwards to Ikaria and Samos islands, and continues into the western part of the Anatolian Menderes Complex (e.g. Jacobshagen, 1986). From bottom to top there are four major tectonic units: (I) a Basement Unit, consisting of pre-Alpine granites, paragneisses and orthogneisses (Ios, Sikinos; van der Maar, 1980), and medium to high-grade metamorphics to migmatites on the central Cyclades (Naxos and Paros; Andriessen et al., 1987; Jacobshagen, 1986 and references therein); (II) the high-pressure/low-temperature Cycladic Blueschist Unit (mainly Syros, Sifnos, Tinos); (III) the Intermediate Unit, made up of metapelites, marbles and metabasites, and present on most of the Cycladic islands (Jansen and Schuiling, 1976; Dürr et al., 1978; Schliestedt et al., 1987); (IV) the uppermost allochthonous Pelagonian Unit with ophiolitic remnants of the Vardar Ocean, located in the hanging wall of the metamorphic core complexes of the northern (Andros, Tinos, Mykonos) and central Cyclades (Naxos and Paros; Jolivet et al., 2013; Huet et al, 2009 and references therein).

Isotopic dating suggests a complex pre-Alpine origin of the basement unit with Variscan (305-295 Ma) and pre-Variscan (~500 Ma) ages (e.g. Henjes-Kunst et al., 1988). The Alpine history of the Cyclades comprises several tectonometamorphic events that have affected the Cycladic Blueschist Unit. Subduction-related Eocene (40-50 Ma) eclogite/blueschist facies metamorphism is well documented (Fig. 1B; e.g. Schmädicke and Will, 2003; Tomaschek et al., 2003; Ring and Layer, 2003). The early exhumation path is characterized by depressurization and cooling (Parra et al., 2002), thus part of the rocks escaped retrogression, especially on Syros Island. However, an Oligo-Miocene (25-16 Ma) Barrovian-type greenschist facies metamorphic overprint is observed in many locations (e.g. Jansen & Schuiling, 1976; Altherr et al., 1982; Henjes-Kunst et al. 1988; Andriessen et al., 1987; Vandenberg and Lister, 1996; Bröcker and Enders, 1999; Huet et al., 2009). The youngest tectonometamorphic history is dominated by extension, caused by the southward retreat of the subducting African slab (e.g. Le Pichon and Angelier, 1979).

Most of Syros is made up of rocks belonging to the Cyclades Blueschist Unit (Fig. 1C), locally called Ermoupoli unit. It mostly dips moderately N to NE (e.g. Rosenbaum et al., 2002; Keiter et al., 2004; 2011) and consists of a strongly tectonized association of gneisses, schists, marbles, serpentinites and metabasites. Most of these are eclogite- to blueschist grade metamorphosed and only locally overprinted by later greenschist grade metamorphism. In the SW part of Syros, around Mavra Vounakia (Fig. 1C) this overprint is more intense, and this led us to avoid sampling there. The schists and marbles are thought of having originated from flysch sediments, whereas the metabasites and serpentinites probably have been part of an ophiolitic mélange (e.g. Dixon and Ridley, 1987; Keiter et al, 2011). Two of these samples (SY1: 37°29'56.86''N/24°53'42.47''E, SY2: 37°29'57.16''N/24°53'35.23''E, SY4) come from the east-west trending blueschist-eclogite belt in the north of the island, near Kambos, near the beaches of Lia and Grammata. Another sample (SY4: 37°24'35.64''N/24°52'32.06''E) is from the bluschist and eclogite occurrence three kilometers north of Finikas in the western part of the island, and the fourth sample (SY5: 37°25'03.18''N/24°57'17.95''E) comes from the southern end of the large blueschist occurrence near the eastern coast south of Ermoupoli (Fig. 1C). These three sampling areas form the largest coherent outcrops of metabasite and sepentinite units on Syros.

3. Methods

CPO measurements were performed at the neutron time-of-flight (TOF) texture diffractometer SKAT at the Frank Laboratory of Neutron Physics (Joint Institute for Nuclear Research in, Dubna, Russia; Keppler et al., 2014; Ullemeyer et al., 1998). Due to the high penetration capability of neutrons in matter and the large beam cross section of the SKAT instrument, measurements of large-volume samples of up to 65 cm^3 are possible, without the need for sample preparation. This allows for good grain statistics even if the investigated samples are coarse-grained. 'Rietveld Texture Analysis' (RTA) was applied for the CPO calculation using the MAUD software (Von Dreele, 1997; Matthies et al. 1997; Lutterotti et al., 1997; Wenk et al., 2010). Low R_{wp} values (5.7-12.4%) were achieved in the RTA for all samples (Von Dreele, 1997). Since RTA requires knowledge of the constituting minerals present in the sample, mineral assemblages and chemical compositions were obtained at the Steinmann-Institute Bonn using a JEOL-JXA-8900 microprobe.
The orientation distribution function (ODF) of each phase, which describes the orientation of the crystal lattice planes related to an external reference frame is finally used to model the elastic properties of the samples applying Christoffel's equation:

$$<C_{ijkl}>n_j n_i - \rho V^2 \delta_{ij} = 0$$

where V is the velocity implying P-waves (Vp) and shear waves (Vs1, Vs2), $<C_{ijkl}>n_j n_i$ the acoustic tensor, C_{ijkl} being the single-crystal stiffness coefficient and n the plane wave propagation direction, ρ is the density and δ_{ijk} is the Kronecker delta. The bulk seismic properties are calculated as weighted averages of the elastic properties of the constituent mineral phases using the ODF and the corresponding single crystal elastic constants. The latter were taken from the literature (omphacite: Bhagat et al., 1992; garnet: Babuska et al., 1978; glaucophane: Bezacier et al., 2010; muscovite: Vaughan and Guggenheim, 1986; quartz: Heyliger et al., 2003; albite: Brown et al., 2006; epidote/zoisite/clinozoisite: Aleksandrov et al., 1974).. The Voigt–Reuss–Hill approximation was used for the calculations because it gives the closest agreement between CPO derived and laboratory-measured seismic velocities (Seront et al., 1989).

4. Microstructure and compostion

The investigated blueschists contain glaucophane (50-60%), clinozoisite (~30%), phengite (5-10%) and minor amounts of garnet,albite and titanite. Since the fraction of retrograde phases is small, this mineral assemblage can be assigned close to peak metamorphic conditions of the PT-path. The blueschists are fine-grained and show a pronounced shape preferred orientation (SPO) of glaucophane and clinozoisite defining the foliation and lineation. Phengite and titanite are also aligned in the foliation, and few sub-idiomorphic albite grains with a random orientation are found within the matrix (Fig. 2A, 3A and 3B). Pressure shadows of garnet mostly contain phengite, could indicate retrograde phengite growth (Fig. 3B; see Table 2A for phengite composition). Inclusions in garnet, which are glaucophane, quartz, rutile and white mica, form a foliation, oblique to the matrix foliation. The glaucophane is rich in Fe and relatively poor in Mg (see Table 1). Lowest Na contents are found in the grain centers, visible as lighter spots in Fig. 3A., arguing for prograde glaucophane growth. Garnets are zoned with increasing almandine and decreasing spessartine contents from core to rim also indicating prograde growth (Fig. 3B). Epidote is composed relatively homogenously and has a high clinozoisite component.

The eclogites are coarse-grained. They contain omphacite (35-45%, Table 2a and 2b), clinozoisite (0-35%), glaucophane (0-20%), phengite (5-20%), garnet (5-10%), quartz (0-15%) and minor amounts of titanite. Sample SY2 shows randomly oriented omphacite with locally interspersed glaucophane (Fig. 2C), indicating local blueschist grade overprinting. Where the fabric is dominated by glaucophane, an SPO is more pronounced (Fig. 2E). The other eclogite sample (SY4) exhibits a strong SPO (Fig. 2D) defining a pronounced foliation and lineation made up by omphacite and glaucophane. Some larger glaucophane grains have been completely replaced by smaller ones presumably indicative of dynamic recrystallization. Phengite commonly has a relatively weak preferred orientation (Fig. 2C), pointing to late stage formation after development of the glaucophane foliation (Fig. 2F). Pressure shadows around garnet contain quartz and phengite (Figs. 2D and 2F). Inclusions in garnets are quartz, white mica and glaucophane. They form a weakly defined foliation fabric oblique to the matrix foliation (Figs. 2D and 2F).

Amphibole in the eclogites is either ferro-eckermannit or ferro-glaucophane (Fig. 2C and Table 2A). The omphacite composition is relatively homogenous within grains (see Fig. 3C for location of microprobe measurements and Table 2B for grain composition), but varies from sample to sample (compare grain compositions in Table 2B and Table 3; see Fig 3D for location of measurements). Omphacite is low in Mg and Ca, and high in Na and Fe. Garnets in the eclogites exhibit a higher almandine component than in the blueschists, but also show increasing almandine and decreasing spessartine contents from core to rim indicating prograde growth (Fig. 3E). White mica in the eclogites is also phengitic (Table 2A) and epidote contains a high clinozoisite component (Table 3).

5. Crystallographic preferred orientation (CPO)

The blueschists show distinct CPO of glaucophane, clinozoisite, and phengite. The [001] axis of glaucophane is either distributed within the foliation plane (Fig. 4; SY1) or forms a point maximum parallel to the mineral lineation (Fig. 4; SY5). Accordingly, [100] forms a maximum normal to the foliation or girdle structures perpendicular to the lineation, representing SL-type and LS-type CPO, respectively. The clinozoisite texture corresponds to that of glaucophane, displaying either S–types with an alignment of [010] in the foliation and a [001] point maximum normal to the foliation, or L-types with an alignment of [010] in lineation direction and [001] girdle structures perpendicular to the lineation. For this interpretation it needs to be taken into account that due to the crystal shape clinozoisite [010] coincides with the glaucophane [001] axis and that clinozoisite [001] coincides with the glaucophane [100] axis. Albite in the blueschists shows a random orientation (not displayed here). Phengite, if present, exhibits a weak alignment of the basal plane parallel to the foliation (Fig. 4). The CPO of all constituent mineral phases has almost orthorhombic symmetry, with the foliation and the plane normal to the lineation being mirror planes.

The eclogites show a distinct CPO of omphacite, glaucophane, clinozoisite and phengite. The [001] axis of omphacite is aligned parallel to the mineral lineation, and the [010] pole figure displays a maximum normal to the foliation with some small rotation around the lineation direction in some samples (Fig. 4; SY2 and SY4). The omphacite CPO is more pronounced in sample SY4 (Fig. 4), an observation that corresponds well to what can be seen as shape preferred orientations in the scanning electron (Fig. 3C, 3D) and optical micrographs (Fig. 2C – 2F). Like for the blueschists, the clinozoisite CPO is geometrically compatible, here with that of omphacite. [010] of clinozoisite is parallel to the mineral lineation, comparable to [001] of omphacite, and [001] of clinozoisite forms a maximum normal to the foliation comparable to [010] of omphacite (Fig. 4; SY4). Glaucophane, when present in substantial amounts (Fig. 4; SY2), depicts an SL-type with weaker alignment of [001] in lineation direction than [001] of omphacite. Glaucophane [100] forms a point maximum normal to the foliation, just as omphacite [010] (Fig. 4). Phengite exhibits an alignment of its basal plane parallel to the foliation similar in topology and intensity to that of the blueschists (Fig. 4). Quartz CPO is weak and garnet displays a random orientation (not displayed here). Like for the blueschists, the CPO of the eclogite constituent mineral phases has the same type of symmetry.

6. Elastic properties

Calculated P-wave velocity (Vp) anisotropy of the blueschists is high, ranging from 6.5% to 12.1% (Table 4). Resulting elastic moduli are given in Table 5. Depending on whether there is a foliation-dominated or a lineation-dominated fabric of glaucophane, maximum Vp is distributed in the foliation (Fig. 5; SY1) or parallel to the lineation direction (Fig. 5; SY5). The lowest Vp is found normal or nearly normal to the foliation. S-wave velocity (Vs) anisotropies are lower, ranging between 0.8 and 7.0%, but still display clear patterns. The foliation-dominated blueschist SY1 has highest Vs1 distributed in the foliation plane, and the maxima for Vs2 are found at the periphery of the pole figure, half way between the foliation normal and the lineation (Fig. 5; SY1). In sample SY5, Vs1 forms two maxima in the foliation plane at angles of about 45° to the lineation. Vs2 maxima are at the periphery of the pole figure between the foliation normal and the lineation (Fig. 5; SY5). Minima of S-wave velocity distributions are also distinct. In samples SY1 and SY5 lowest Vs1 velocity is oriented normal or nearly normal to the foliation. Lowest Vs2 in sample SY1 is located near the lineation, with a secondary minimum normal to the foliation. In blueschist sample SY5 Vs2 displays two minima in a girdle perpendicular to the lineation. In sample SY5, the anisotropy of Vs2 is slightly higher than that of Vs1. In contrast, in sample SY1, the anisotropy of Vs1 is well above the one of Vs2 (7.0 versus 2.4%). Vp/Vs ratios of the blueschist samples were calculated using the mean Vp and Vs velocities, and vary between 1.71 and 1.76 (Table 4).

With values of 3.3% and 3.7% the Vp anisotropy of the eclogites (Table 4) is lower by a factor of two to three than that in the blueschists. Resulting elastic moduli are given in Table 5. Both eclogite samples show highest Vp in the lineation direction and lowest Vp normal to the foliation (Fig. 5 SY2 and SY4). Vs anisotropy lies between 0.8% and 2%. Two maxima of Vs1 occur in the foliation plane at about 45° to the lineation, and Vs1 minima are aligned with the foliation normal (Fig. 5, SY2 and SY4). For Vs2, maxima are at the periphery of the pole figure between the foliation normal and the lineation. Vs2 minima form a girdle distribution in sample SY2. In sample SY4 one minimum is parallel to the foliation normal, and a secondary minimum aligned with the lineation and smeared out along the foliation plane (Fig. 5, SY2 and SY4). The Vp/Vs ratio of the eclogite samples, calculated using the mean Vp and Vs velocities, is 1.69 to 1.70 (Table 4).

7. Discussion

The question whether mineralogical composition of subducted oceanic crust is capable of defining or modifying the seismic image of subduction zones will be the starting point of this discussion. There are two major methods for seismic investigation. In seismic tomography large rock volumes can be investigated and data on seismic velocities and anisotropies are usefull to compare subducted oceanic crust with the surrounding mantle peridotites. In reflection seismology, smaller scales, like the tectonic setting of a subduction channel are considered. Recent numerical simulations of seismic wave propagation modeled a detailed subduction channel structure with mafic blocks in a serpentinite matrix (Friedrich et al., 2014).

Generally speaking blueschists have a stability field with a lower pressure bound of about 5-6 kbar, (e.g. Bousquet et al., 2008) in a regime of low geothermal gradients. This translates to a depth in a subducted slab of about 15-18 km. Beyond a pressure of about 10 kbar, i.e. a depth of about 30 km, conversion of blueschist to eclogite is expected to occur, principally involving breakdown of glaucophane and paragonite (e.g. Winter, 2001) on the prograde path of metamorphism, a process that can be documented on Syros (e.g. Okrusch et al., 1978; Schliestedt, 1986; Rosenbaum et al., 2002; Schmädicke and Will, 2003). The persistence of prograde glaucophane (Fig. 3A) in the eclogites (Figs. 2C, 2D) indicates that this breakdown did probably not proceed completely, until peak pressures of around 20 kbar were attained (see Fig. 1C, and Jolivet and Brun, 2010).

Several recent numerical studies have been proposing tectonic overpressure as a major component influencing metamorphic conditions, which would indicate that many previous studiesassuming lithostatic pressures might not be correct (e.g. Burg and Gerya, 2005; Mancktelow, 2008; Angel et al., 2015; Gerya, 2015). The main factor influencing tectonic overpressure in these models is the rheology dependent heterogeneity in deforming rock units. The extent of the influence of tectonic overpressure suggested in these models, however, is not widely accepted among metamorphic

petrologists. Klonowska et al. (2017) for example showed that in the Seve Nappe of the Scandinavian Caledonides both, strong eclogites, peridotites and the surrounding weak gneissic matrix yield evidence for ultra-high pressure conditions. According to the previously mentioned numerical models, on the other hand, this rheology contrast should have led to enormous tectonic overpressure and/or underpressure, which have not been detected. Before this and other inconsistencies between petrological data and tectonic overpressure models have not been clarified, we prefer adhere to the classical concept assuming only lithostatic pressures in the present study. As this assumption does not affect our data, the presented results could be (re-)interpreted at any later point of time.
There might be some uncertainty regarding the depth and extent of the transition zone from blueschists to eclogites, a general picture can be drawn regarding the seismic characteristics of subducted oceanic crust depending on depth. Below a depth of 15 km, subducted oceanic crust would be highly anisotropic (6-12 %) because of the presence of prograde blueschists with strong CPO. Comparably strong seismic anisotropies have been documented in blueschists from elsewhere before (Bezacier et al., 2010; Ha et al., 2016) and seem to be a widespread characteristic of such metamorphic belts. Blueschists making up subducted oceanic crust can also be identified by average shear wave velocities below about 4.5 km/s, and variable shear wave splitting depending on the intensity of deformation and, thus, seismic anisotropy (see Table 4).

Our observations and data regarding compositional and textural changes suggest that anisotropy in subducted oceanic crust would start vanishing below about 30 km due to progressive eclogitization, mainly because eclogites have much lower seismic anisotropy (1.5-3 % texture-induced contribution). This is an observation that has also been reported by studies from other subduction complexes (e.g. Mauler et al., 2000; Keppler et al., 2015). Velocity, and Vp/Vs signature of the Syros samples is also very similar to that of other eclogites (e.g. Keppler et al., 2015). Apparently, Vp/Vs can be changed to higher values by retrograde transformation of eclogites to amphibolites (e.g. Gao et al., 2001; Keppler et al., 2015), probably owing to the growth of lower-pressure hornblende, but this is not an issue in the samples of this study. Moreover, this is a process unlikely to occur in subducted oceanic crust at great depth, but may, of course, alter the seismic signature of ophiolite complexes as they are exhumed and tectonically emplaced at higher levels in the crust.

Following a discussion of Keppler et al. (2015) the Vp/Vs values of the blueschists and eclogites are lower than those of peridotites of the lithospheric mantle of a downgoing slab in global earth models (e.g. Kennett et al., 1995) and experimental work (e.g., Christensen, 1966, 2004; Kern, 1993; Ullemeyer et al., 2010). In a tomographic study of subducting slabs off Northern Honshu Zhang et al. (2004) concluded that the downgoing peridotite slab has Vp/Vs ratios of 1.80–1.85 at depths between 60 and 85 km, and is overlain by a zone of lower Vp/Vs ratios (1.70–1.80). This zone was interpreted to reflect subducted metagabbros of the oceanic crust that are transformed to blueschists and eclogites at depth. Our results corroborate this interpretation, and add the notion that blueschists may be visible in seismic velocity models on grounds of their pronounced anisotropy.

An interesting aspect lies in the observation that both, the eclogite and the blueschist samples show variations in fabric topology, indicating different strain histories that the samples experienced while being subducted (see e.g. discussion by Keppler et al., 2016). In the SL-type blueschist sample highest Vp is distributed within the foliation plane. The pattern is determined by the glaucophane CPO, showing a distribution of [001] within the foliation plane, which is the crystal axis closest to highest Vp in glaucophane single crystals. The LS-type blueschist produces highest Vp in the lineation direction, which is in line with an alignment of glaucophane [001] parallel to the lineation of this sample. A similar pattern for Vp is observed in the eclogite samples. For these, omphacite [001], the vector closest to highest Vp in omphacite single crystals, is aligned parallel to the lineation, yielding maximum Vp in the same direction. Garnet shows a random CPO, but due to its high Vp and Vs generally increases the average velocities of the samples. White mica can strongly influence the elastic anisotropy of rocks, even with low volume percentages (Mainprice and Ildefonse, 2009). However, because of its weak CPO it is a minor contributor to anisotropy in the studied samples. Based on the small sample set, however, we cannot demonstrate that strain variations are characteristic for the entire deformation path (e.g.,Abalos 1997; Abalos et al., 2011; Keppler et al., 2016), i.e. whether texture evolution followed a distinct spatial or temporal pattern (e.g., Kurz, 2005).

In the calculation of the elastic properties minor errors may be introduced by compositional differences of the minerals in our samples relative to those of the single crystal data used for modelling. Our measurements show that there are not only grain-to-grain differences in mineral chemistry within a sample but also within individual grains (Tables 1-3). Volume percentages were determined by ‘Rietveld Refinement’, which is not as exact as powder diffraction. However, these minor errors in mineral volume fractions produced using ‘Rietveld Refinement’ do not effect calculated elastic anisotropies. Further errors could have been caused by the fact that the single crystal elastic tensors are taken from measurements under ambient conditions. Some influence of pressure and temperature can be expected beyond pressures of 10 kbar. Comparison of modelled and experimentally measured data frequently shows higher values for the measured elastic anisotropies (e.g., Kern et al., 2008; Keppler et al., 2015). The velocity patterns (i.e. location of minima and maxima), however, usually are similar in measured and modelled results. Also, inaccuracy in the CPO determination is a possible error source for the calculation of the elastic anisotropy. On the other hand Keppler et al. (2014) demonstrated that even for polyphase rock samples TOF texture analysis, using RTA, leads to reliable CPO results with only minor differences in texture strength. In this study the influence of incompletely closed microcracks on the elastic anisotropy (e.g. Ullemeyer et al., 2011) was not considered. When considering material behaviour at subduction zone depth, however, it is more likely that microcracks in the subduction slab are generally closed. Elastic properties calculated from CPO could, therefore, approximate the elastic properies of crack-closed rocks at depth.

8. Conclusions

Knowledge of the elastic properties of subducted oceanic crust is important for seismic investigations on active subduction zones. In this study we examined exhumed slices of blueschists and eclogites, which were subducted as part of the Hellenic subduction system and are now exposed on the island of Syros. Based on neutron texture measurements and modelling of the elastic anisotropies of the paleo-subduction zone rocks and their constituting minerals we can conclude:

1. Blueschists show larger elastic anisotropy than eclogites due to a higher single crystal elastic anisotropy of glaucophane. Accordingly, eclogites will exhibit larger elastic anisotropies if glaucophane is present.
2. The contrasting seismic properties (e.g. much higher elastic anisotropy in the blueschists compared to the eclogites) might permit the distinction between blueschists, eclogites, and possibly glaucophane-bearing eclogites in seismic imaging of subduction zones.
3. As blueschists generally occur at shallower depths than eclogites, our data imply a depth dependence of seismic anisotropy in a subducted oceanic crustal slab. In any quantification of this depth dependence, however, it needs to be considered that there is a depth range where eclogite and blueschist stabilities might overlap.

ACKNOWLEDGEMENTS:

We kindly thank Tatiana Ivankina and Benito Abalos for their constructive and very helpful comments. We are also grateful to the late Klaus Ullemeyer for his help performing the texture measurements. Michael Marks and Lisa Vielstaedter are thanked for providing insights on Syros eclogites and blueschists during discussions in the field. Funding by the German Federal Ministry of Education and Research (BMBF) is gratefully acknowledged. We also would like to thank the Frank Laboratory of Neutron Physics (FLNP) at Dubna (Russia) for support in the texture measurements. All time-of-flight spectra used for the calculations can be found on https://uni-bonn.sciebo.de/index.php/s/mSboAvg8hdwvNZw.

REFERENCES

Ábalos, B., 1997. Omphacite fabric variation in the Cabo Ortegal eclogite (NW Spain): Relationships with strain symmetry during high-pressure deformation. Journal of Structural Geology, 19, 621-637.

Ábalos, B., Fountain, D.M., Gil Ibarguchi, J.I. and Puelles, P., 2011. Eclogite as a seismic marker in subduction channels: Seismic velocities, anisotropy, and petrofabric of Cabo Ortegal eclogite tectonite (Spain). Geological Society of America Bulletin, 123, 439-456.

Abalos, B., Puelles, P., Gil Ibarguchi, J.I., 2003. Structural assemblage of high-pressure mantle and crustal rocks in a subduction channel (Cabo Ortegal, NW Spain). Tectonics 22 (2), 1006, doi: 10.1029/2002TC001405.

Abers, G.A., 2005. Seismic low-velocity layer at the top of subducting slabs: observations, predictions, and systematics. Physics of the Earth and Planetary Interiors, 149, 7–29.

Aleksandrov, K.S., Alchikov, U.V., Belikov, B.P., Zaslavski, B.I., and Krupny, A.I., 1974. Elastic wave velocities in minerals at atmospheric pressure and increasing precision of elastic constants by means of EVM. Izvestija Academy of Science USSR, Geological Series, 10, 15-24.

Altherr, R., Kreuzer, H., Wendt, I., Lenz, H., Wagner, G.A., Keller, J., Harre, W. and Hohndorf, A., 1982. A late Oligocene/early Miocene high temperature belt in the Attic-Cycladic crystalline complex (SE Pelagonian, Greece): Geologisches Jahrbuch, 23, 97–164.

Andriessen, P. A. M., Banga, G. and Hebeda, E.H., 1987. Isotopic age study of pre-Alpine rocks in the basal units on Naxos, Sikinos and Ios, Greek Cyclades, Geologie van de Mijnbouw, 66, 3–14.

Audet, P., Bostock, M.G., Christensen, N.I. and Peacock, S.M., 2009. Seismic evidence for overpressured subducted oceanic crust and megathrust fault sealing. Nature, 457, 76-78.

Babuska, V., Fiala, J., Kumazawa, M., Ohno, I., and Sumino, Y., 1978. Elastic properties of garnet solid-solution series. Physics of the Earth and Planetary Interiors, 16, 157–176.

Bascoua, J., Barruol, G., Vauchez, A., Mainprice, D. and Egydio-Silva, M., 2001. EBSD-measured lattice-preferred orientations and seismic properties of eclogites. Tectonophysics, 342, 61– 80.

Behr, W.M., Platt, J.P., 2013. Rheological evolution of a Mediterranean subduction complex. Journal of Structural Geology, 54, 136-155.

Behrmann, J.H., Ratschbacher, L., 1989. Archimedes revisited. A structural test of eclogite emplacement models in the Austrian Alps. Terra Nova, 1, 242-252.

Bezacier L., Reynard B., Bass J.D., Wang J., Mainprice D., 2010. Elasticity of glaucophane, seismic velocities and anisotropy of the subducted oceanic crust. Tectonophysics 494, 201-210.

Bhagat, S.S., Bass, J.D., and Smyth, J.R., 1992. Single-crystal elastic properties of omphacite-C2/C by Brillouin spectroscopy. Journal of Geophysical Research–Solid Earth, 97, 6843–6848.

Bousquet, R., El Mamoun, R., Saddiqi, O., Goffé, B., Möller, A., and Madi, A. , 2008. Mélanges and ophiolites during the Pan-African orogeny: the case of the Bou-Azzer ophiolite suite (Morocco) Geological Society, London, Special Publications, 297, 233-247, doi:10.1144/SP297.11

Bröcker, M. and Enders, M., 1999. U–Pb zircon geochronology of unusual eclogite-facies rocks from Syros and Tinos (Cyclades, Greece). Geological Magazine, 136(2), 111–118.

Brown, J. M., Abramson, E. H. and Angel, R. J., 2006. Triclinic elastic constants for low albite. Physics and Chemistry of Minerals, 33, 4, 256-265.

Burg, J.-P. and Gerya, T., 2005. Viscous heating and thermal doming in orogenic metamorphism: numerical modeling and geological implications. Journal of Metamorphic Geology, 23, 75–95.

Christensen, N.I., 1965. Compressional wave velocities in metamorphic rocks at pressures to 10 kilobars. Journal of Geophysical Research 70(24), 6147-6164.

Christensen, N.I., 1966. Elasticity of ultrabasic rocks. Journal of Geophysical Research, 71, 5921–5931.

Christensen, N.I., 2004. Serpentinites, Peridotites, and Seismology. International Geology Review 46 (9), 795-816.

Christensen, N.I. and Fountain, D.M., 1975: Constitution of the lower continental crust based on experimental studies of seismic velocities in granulite. Geological Society of America Bulletin 86(2), 227-236.

Dixon, J.E., Ridley, J., 1987. Syros. In: Helgeson, H.C., (Ed.), Chemical Transport in Metasomatic Processes, Reidel Publishing Company, Dordrecht, 489–501.

Dürr, S., Seidel, E., Kreuzer, H. and Harre, W., 1978. Témoins d'un métamorphisme d'âge crétacé supérieur dans l'Egéide: Datations radiométriques de minéraux provenant de l'île de Nikouria (Cyclades, Grèce), Bulletin Géologique de la Société Francaise, 20, 209–213.

Essen, K., Braatz, M., Ceranna, L., Friederich W. and Meier, T., 2009. Numerical modelling of seismic wave propagation along the plate contact of the Hellenic Subduction Zone—the influence of a deep subduction channel. Geophysical Journal International 179, 1737–1756.

Ernst, W.G., 1988. Tectonic history of subduction zones inferred from retrograde blueschist *P-T* paths. Geology, 27, 103-106.

Fountain, D.M., Boundy, T.M., Austrheim, H., and Rey, P., 1994. Eclogite-facies shear zones—Deep crustal reflectors? Tectonophysics, 232, 411–424.

Friederich, W., Lambrecht, L., Stöckhert, B., Wassmann, S. and Moos, C., 2014. Seismic visibility of a deep subduction channel – insights from numerical simulation of high-frequency seismic waves emitted from intermediate depth earthquakes. Solid Earth, 5, 141–159.

Fryer, P., Wheat, C.G., Mottl, M.J. 1999. Mariana blueschist mud volcanism: Implications for conditions within the subduction zone. Geology, 16, 1081-1084.

Gao, S., Kern, H., Jin, Z., Popp, T., Jin, S., Zhang, H., and Zhang, B., 2001. Poisson's ratio of eclogite: the role of retrogression. Earth Planet. Sci. Lett. 102, 523–531.

Gautier, P. and Brun, J.-P., 1994. Crustal-scale geometry and kinematics of late-orogenic extension in the central Aegean (C&lades and Ewia Island). Tectonophysics 238, 399-424.

Gautier, P., Brun, J.-P. and Jolivet, L., 1993. Structure and kinematics of Upper Cenozoic extensional detachment on Naxos and Paros (Cyclades Islands, Greece). Tectonics, 12, 5, 1180 -1194.

Ha, Y., Jung, H. and Raymond L.A., 2016. Deformation fabrics of blueschist facies phengite-rich, epidote-glaucophane schists from Ring Mountain, California and implications for seismic anisotropy in subduction zone. Abstract, AGU Fall Meeting, T31E-2955

Helffrich, G.,Stein,S.,1993. Study of the structure of the slab-mantle interface using reflected and converted seismic waves. Geophys.J.Int.115,14–4072.

Henjes-Kunst, F., Altherr, R., Kreuzer, H. and Hansen, B.T., 1988. Disturbed U-Th-Pb systematics of young zircons and uranothorites: The case of the Miocene Aegean granitoids (Greece): Chemical Geology, 73, 125–145.

Heyliger, P., Ledbetter, H., Kim, S., 2003. Elastic constants of natural quartz. Journal of the Acoustical Society of America, 114, 644-650.

Huet, B., Labrousse, L., and Jolivet, L., 2009. Thrust or detachment? Exhumation processes in the Aegean: Insight from a field study on Ios (Cyclades, Greece): Tectonics, 28, TC3007, doi: 10.1029 /2008TC002397.

Jacobshagen, V., 1986. Geologie von Griechenland. Gebrüder Bornträger, Berlin 363 pp.

Jansen, J.B.H. and Schuiling, R.D., 1976. Metamorphism on Naxos: Petrology and geothermal gradients: American Journal of Science, 276, 1225–1253.

Ji, S., Saruwatari, K., Mainprice, D., Wirth, R., Xu, Z. and Xia B., 2003. Microstructures, petrofabrics and seismic properties of ultra high-pressure eclogites from Sulu region, China: implications for rheology of subducted continental crust and origin of mantle reflections. Tectonophysics, 370, 49–76.

Ji, S. and Zhao, P., 1994: Layered rheological structure of subducting oceanic lithosphere. Earth Planet. Sci. Lett., 124: 75-94.

Ji, S., Wang, Z. and Saruwatari, K., 1998: Plasticity of eclogite: implications for rheology and seismic reflectivity of the subducting slab. LITHOPROBE Report nº 64: 86-91.

Jolivet, L., Faccenna, C., Goffé, B., Burov, E., Agard, P., 2003. Subduction tectonics and exhumation of high-pressure metamorphic rocks in the Mediterranean orogens. American Journal of Science, 303, 353–409.

Jolivet, L., Faccenna, C., Huet, B., Labrousse, L., Le Pourhiet, L., Lacombe, O., Lecomte, E., Burov, E., Denele, Y., Brun, J.P., Philippon, M., Paul, A., Salaun, G., Karabulut, H., Piromallo, C., Monie, P., Gueydan, F., Okay, A., Oberhansli, R., Pourteau, A., Augier, R., Gadenne, L . and Driussi, O., 2013. Aegean tectonics: Strain localisation, slab tearing and trench retreat. Tectonophysics, 597, 1 -33.

Keiter, M., Ballhaus, C. and Tomaschek, F., 2011. A new geological map of the Island of Syros (Aegean Sea, Greece): implications for lithostratigraphy and structural history of the Cycladic blueschist unit. Geological Society of America Special Paper, 481, 43 pp.

Keiter, M., Piepjohn, K., Ballhaus, C., Lagos, M. and Bode, M, 2004. Structural development of high-pressure metamorphic rocks on Syros island (Cyclades, Greece). Journal of Structural Geology, 26, 8, 1433 -1445

Kennett, B.L.N., Engdahl, E.R. and Buland, R., 1995. Constraints on seismic velocities in the Earth from travel times. Geophys. J. Int. 122, 108–124.

Keppler, R., Stipp, M., Behrmann, J.H., Ullemeyer, K. & Heidelbach, F., 2016. Deformation inside a paleosubduction channel – Insights from microstructures and crystallographic preferred orientations of eclogites and metasediments from the Tauern Window, Austria. Journal of Structural Geology, 82, 60-79.

Keppler, R., Ullemeyer, K., Behrmann, J.H. & Stipp, M., 2014. Potential of full pattern fit methods for the texture analysis of geological materials: implications from texture measurments at the recently upgraded neutron time-of-flight diffractometer SKAT. Journal of Applied Crystallography, 47, 1520-1535.

Keppler, R., Ullemeyer, K., Behrmann, J.H., Stipp, M., Kurzawski, R. & Lokajíček, T., 2015. Crystallographic preferred orientations of exhumed subduction channel rocks from the Eclogite Zone of the Tauern Window (Eastern Alps, Austia), and implications on rock elastic anisotropies at great depths. Tectonophysics, 647, 89-104.

Kern, H., 1978. The effect of high temperature and high confining pressure on compressional wave velocities in quartz-bearing and quartz-free igneous and metamorphic rocks. Tectonophysics, 44, 185-203.

Kern, H., 1993. P- and S-wave anisotropy and shear-wave splitting at pressure and temperature in possible mantle rocks and their relation to the rock fabric. Physics of the Earth and Planetary Interiors 78, 245-256.

Kern, H., Ivankina, T.I., Nikitin, A.N., Lokajíček, T., Pros, Z., 2008. The effect of oriented microcracks and crystallographic and shape preferred orientation on bulk elastic anisotropy of a foliated biotite gneiss from Outokumpu. Tectonophysics, 457, 143–149.

Kim, D., Katayama, I., MIchibayashi. K. and Tsujimori. T., 2013. Deformation fabrics of natural blueschists and implications for seismic anisotropy in subducting oceanic crust. Physics of the Earth and Planetary Interiors 222, 8–21.

Klonowska, I., Janak, M., Majka, J., Petrík, I., Froitzheim, N. Gee, D.G. and Sasinkova, V., 2017. Journal of Metamorphic Petrology. doi:10.1111/jmg.12244

Kurz, W., 2005. Constriction during exhumation: Evidence from eclogite microstructures. Geology, 33, 1, 37-40.

Le Pichon, X. and Angelier, J., 1979. The Hellenic Arc and Trench System: A Key tot he Neotectonic Evolution of the Eastern Mediterranean. Tectonophysics, 60, 1-42.

Lutterotti, L., Matthies, S., Wenk, H.-R., Schultz, A. J., and Richardson, J. W., 1997. Combined texture and structure analysis of deformed limestone from time-of-flight neutron diffraction spectra. Journal of Applied Physics 81, 594–600.

Maekawa, H., Shozu,l M., Ishll, T., Fryer, P., Pearce, J.A., 1993. Blueschist metamorphism in an active subduction zone. Nature, 364, 520-523.

Mainprice, D., and Ildefonse, B., 2009. Seismic Anisotropy of Subduction Zone Minerals–Contribution of Hydrous Phases. In: S. Lallemand and F. Funiciello (eds.), Subduction Zone Geodynamics, Springer-Verlag Berlin Heidelberg, 63-84.

Malusá, M.G., Faccenna, C., Garzanti, E., Polino, R., 2011. Divergence in subduction zones and exhumation of high pressure rocks (Eocene Western Alps). Earth and Planetary Science Letters, 310, 21-32.

Mancktelow, N.S., 2008. Tectonic pressure: theoretical concepts and modelled examples. Lithos, 103, 149–177.

Maruyama, S., Liou, J.G., Terabayashi, M. 1996. Blueschists and eclogites of the world and their exhumation. International Geology Review, 38, 485–594.

Matthies, S., Lutterotti, L. and Wenk, H.-R., 1997. Combined texture and structure analysis of deformed limestone from time-of-flight neutron diffraction spectra. Journal of Applied Crystallography, 28, 254-266.

Mauler, A., Burlini, L., Kunze, K., Philippot, P., and Burg, J.-P., 2000. P-wave anisotropy in eclogites and relationship to the omphacite crystallographic fabric. Phys. Chem. Earth 15, 119–126.

Okrusch, M., Seidel, E., Kreuzer, H., Harre, W., 1978. Jurassic age of metamorphism at the base of the Brecovica peridotite (Yugoslavia). Earth and Planetary Science Letters, 39, 291–297.

Parra, T., Vidal, O. and Jolivet, L., 2002. Relation between the intensity of deformation and retrogression in blueschist metapelites of Tinos Island (Greece) evidenced by chlorite–mica local equilibria. Lithos 63, 41-66.

Platt, J.P., 1993. Exhumation of high-pressure rocks: a review of concept and processes. Terra Nova 5, 119–133.

Ring, U., Glodny, J., Will, T. and Thomson, S., 2010. The Hellenic Subduction System: High-Pressure Metamorphism, Exhumation, Normal Faulting, and Large-Scale Extension. Annual Reviews of Earth and Planetary Science, 38, 45-76.

Ring, U. and Layer, P.W., 2003. High-pressure metamorphism in the Aegean, eastern Mediterranean: Underplating and exhumation from the Late Cretaceous until the Miocene to Recent above the retreating Hellenic subduction zone. Tectonics, 22, 3, doi:10.1029/2001TC001350.

Ring, U., Thomson S.N. and Bröcker, M., 2003. Fast extension but little exhumation: the Vari detachment in the Cyclades, Greece. Geological Magazine, 140, 3, 245-252.

Roche, V., Laurent, V., Cardello, G.L., Jolivet, L. and Scaillet, S., 2016. Anatomy of the Cycladic

Blueschist Unit on Sifnos Island (Cyclades, Greece). Journal of geodynamics, 97, 62 -87.

Rosenbaum G, Avigad D, Sanchez-Gomez M (2002) Coaxial flattening at deep levels of orogenic belts: evidence from blueschists and eclogites on Syros and Sifnos (Cyclades, Greece). Journal of Structural Geology, 24, 1451–1462.

Schliestedt, M., Altherr, R. and Mattews, A., 1987. Evolution of the Cycladic crystalline complex: Petrology, isotope geochemistry and geochronology, in Chemical Transport in Metasomatic Processes, edited by H. C. Helgerson, pp. 389–428, D. Reidel, Dordrecht, Netherlands.

Schmädicke, E. and Will, T.M. 2003. Pressure-temperature evolution of blueschist facies rocks from Sifnos,Greece, and implications for the exhumation of high-pressure rocks in the central Aegean. Journal of Metamorphic Geology, 21, 799-811.

Seront, B., Mainprice, D., Christensen, N.I., 1989. The complete seismic properties of an anorthosite: comparison between LPO and laboratory measurements. EOS 70, 460–461.

Tomaschek, F., Kennedy, A., Villa, I.M., Lagos, M., Ballhaus, C., 2003. Zircons from Syros, Cyclades, Greece—recrystallization and mobilisation during high-pressure metamorphism. Journal of Petrology, 44, 1977–2002.

Trotet, F., Jolivet, L. and Vidal, O., 2001a. Tectono-metamorphic evolution of Syros and Sifnos islands (Cyclades, Greece). Tectonophysics, 338, 179–206.

Trotet, F., Vidal, O., Jolivet, L., 2001b. Exhumation of Syros and Sifnos metamorphic rocks (Cyclades, Greece). New constraints on the P-T paths. European Journal of Mineralogy, 13, 901–920.

Ullemeyer, K., Leiss, B., Stipp, M., 2010. Textures and Microstructures in Peridotites from the Finero Complex (Ivrea Zone, Alps) and their Influence on the Elastic Rock Properties. Solid State Phenomena 160, 183-188.

Ullemeyer, K., Nikolayev, D.I., Christensen, N.I., Behrmann, J.H., 2011. Evaluation of intrinsic velocity–pressure trends from low-pressure P-wave velocity measurements in rocks containing microcracks. Geophys. J. Int. 185, 1312–1320.

Ullemeyer, K., Siegesmund, S., Rasolofosaon, P.N.J., Behrmann, J.H., 2006. Experimental and texture-derived P-wave anisotropy of principal rocks from the TRANSALP traverse: an aid for the interpretation of seismic field data. Tectonophysics, 414, 97-116.

Ullemeyer, K., Spalthoff, P., Heinitz, J., Isakov, N. N., Nikitin, A. N., Weber, K., 1998. The SKAT texture diffractometer at the pulsed reactor IBR-2 at Dubna: Experimental layout and first measurements. Nuclear Instruments and Methods of Physical Research, 412, 80–88.

Vandenberg, L. C., and Lister, G.S., 1996. Structural analysis of basement tectonics from the Aegean metamorphic core complex of Ios, Cyclades, Greece. Journal of Structural Geology, 18, 1437–1454.

van der Maar, P., 1980. The geology and petrology of Ios, Cyclades, Greece, Ann. Geol. Pays Helleniques, 30, 206–224.

Vaughan, M.T, Guggenheim, S., 1986. Elasticity of muscovite and its relationship to crystal structure. Journal of Geophysical Research 91, 4657– 4664.

Von Dreele, R.B., 1997. Quantitative texture analysis by Rietveld refinement. Journal of Applied Crystallography, 30, 577-587.

Wakabayashi, J. 1999. Subduction and the rock record: Concepts developed in the Franciscan Complex, California, in Moores EM, Sloan D, Stout DL (eds), Classic Cordilleran Concepts: A View from California: Boulder, Colorado, Geological Society of America Special Paper, 338, 123-133.

Wakabayashi, J., Tsujimori, T., Ogawa, Y., Shervais, J., 2015. Convergent plate margin processes and their rock record. International Geology Review, 57 (5-8), v-ix, DOI: 10.1080/00206814.2015.1026415
Wenk, H.-R., Lutterotti, L. and Vogel, S. C., 2010. Rietveld texture analysis from TOF neutron diffraction data. Powder Diffraction 25, 3, 283-296.

Wenk, H.-R., Lutterotti, L. and Vogel, S. C., 2010. Rietveld texture analysis from TOF neutron diffraction data. Powder Diffraction 25, 3, 283-296.

Winter, J.D., 2001. An introduction to igneous and metamorphic petrology. Prentice Hall, New Jersey, 687 pp.

Zhang, H., Thurber, C.H., Shelly, D., Ide, S., Beroza, G.C. and Hasegawa, A., 2004. High resolution subducting-slab structure beneath northern Honshu, Japan, revealed by double-difference tomography. Geology 42, 361–364. http://dx.doi.org/10.1130/G20261.2.

Table 1: Microprobe measurements of glaucophane in blueschist sample SY1. See Fig. 3A for location of measurements.

Sy1_gl_line

SiO2	58.158	57.466	56.294	54.942	52.82	57.289	57.787	57.82	58.212	57.972	57.791
TiO2	0.019	0.034	0.111	0.069	0.157	0.045	0.016	0.05	0.069	0.079	0.074
Al2O3	11.319	11.432	11.619	11.015	9.591	11.412	11.334	11.366	11.425	11.492	11.307
Cr2O3	0	0.031	0.008	0.01	0	0.013	0.013	0.023	0.045	0.028	0
FeO	9.537	9.868	9.853	10.784	11.213	10.011	9.399	9.296	9.756	10.233	9.466
MnO	0	0.043	0.086	0.038	0.081	0.059	0.005	0.032	0.021	0.086	0.07
MgO	10.628	10.505	10.446	11.178	12.625	10.414	10.699	10.299	10.493	10.417	10.628
CaO	0.815	1.154	2.253	3.83	6.882	1.261	0.888	0.597	0.76	0.99	0.972
Na2O	7.096	6.987	6.407	5.456	3.93	6.949	7.293	7.414	7.086	6.839	7.26
K2O	0.004	0.017	0.075	0.1	0.213	0.017	0.015	0.01	0.013	0.012	0.009
sum	97.576	97.537	97.152	97.422	97.512	97.47	97.449	96.907	97.88	98.148	97.577

Si	7.9308403787	7.8689316226	7.7885144776	7.6229346084	7.4227544777	7.8620079286	7.9093375001	7.9604027497	7.9172959388	7.8703556105	7.908989659
Al	0.0691596213	0.1310683774	0.2114855224	0.3770653916	0.5772455223	0.1379920714	0.0906624999	0.0395972503	0.0827040612	0.1296443895	0.091010341
Al	1.7499040421	1.7137648479	1.6830003339	1.4240117901	1.0111574191	1.7076780927	1.7375356292	1.8045461907	1.7485586809	1.7090171105	1.7326261895
Fe(iii)	0.200534365	0.2105648794	0.1048575851	0.3136895254	0.3518106668	0.1970343899	0.1501927657	0.0654540387	0.2230398076	0.3114112786	0.1303371526
Ti	0.0019487459	0.003501673	0.0115506751	0.0072004342	0.0165942726	0.0046447957	0.001647107	0.0051774847	0.0070583846	0.0080666838	0.0076170075
Cr	0	0.0033559185	0.000875039	0.0010968889	0	0.0014104266	0.0014066894	0.0025033968	0.0048386229	0.0030052389	0
Fe(ii)	0.8869541526	0.9193275411	1.0350355996	0.9374356422	0.9658138663	0.9517614358	0.9255161301	1.0047244578	0.8864908356	0.8502571807	0.9529172179
Mn	0	0.0049866857	0.0100769642	0.0044651913	0.009640298	0.0068572974	0.0005795871	0.0037311755	0.0024189249	0.0098881094	0.0081133008
Mg	2.1606586944	2.1444984545	2.1546038032	2.3121005279	2.6449834772	2.130613562	2.1831220915	2.1138632559	2.1275947436	2.1083543982	2.1683891316
Ca	0.119066414	0.1692904778	0.3339455291	0.5692963806	1.0361038467	0.1853955226	0.1302101514	0.0880548342	0.1107388143	0.1439902832	0.1425111951
Na	1.8759951036	1.8548290708	1.7185239717	1.4675754533	1.0706994927	1.848812613	1.9351940512	1.9788728186	1.8684171876	1.8000187282	1.9262194628

K	0.0006957909	0.0029693592	0.0132361842	0.0176981042	0.0381817051	0.0029759126	0.0026188477	0.0017561676	0.0022553644	0.0020780995	0.0015711307
TOTAL	14.9957573085	15.0270889079	15.065705685	15.0545699381	15.1449850445	15.0371840483	15.0680230502	15.0686838205	14.9814113664	14.9460871109	15.0703017886

Table 2: Microprobe data of (A) amphibole and white mica; (B) omphacite in eclogite sample SY2. See Fig. 3C for location of measurements.

Sy2 amp line

	1	2	3	4	5	6	7	8	9	10	11	12	13	14	15	16	17
SiO_2	47.734	50.909	49.883	47.559	50.786	50.599	50.743	50.667	51.081	50.891	50.387	50.753	50.673	50.725	51.428	49.923	50.62
TiO_2	0.202	0.172	0.311	0.221	0.261	0.227	0.224	0.254	0.182	0.227	0.245	0.166	0.232	0.264	0.214	0.243	0.243
Al_2O_3	27.289	28.512	28.541	27.561	28.414	28.773	29.223	28.549	28.66	28.763	28.643	28.522	28.775	27.926	28.643	28.117	28.347
Cr_2O_3	0	0	0	0	0	0.028	0.022	0	0.008	0.015	0.013	0.01	0	0.036	0.005	0	0
FeO	8.659	5.064	5.13	5.433	4.969	5.101	4.753	4.403	4.555	4.438	5.362	4.869	4.639	4.963	4.878	5.438	5.006
MnO	0.04	0	0	0	0.01	0	0.025	0	0.041	0.015	0.03	0.01	0	0	0.046	0	0.086
MgO	1.937	1.967	1.823	1.76	2.122	1.571	1.956	2.061	2.051	1.978	1.903	1.965	2.004	2.056	1.995	1.809	2.02
CaO	0.089	0	0.006	0.131	0	0	0.001	0	0.006	0.007	0	0.03	0.008	0	0	0.01	0
Na_2O	0.339	0.371	0.46	0.397	0.72	0.225	0.417	0.418	0.386	0.455	0.379	0.371	0.522	0.451	0.417	0.38	0.509
K_2O	10.387	11.062	10.793	10.288	10.835	11.171	11.098	11.002	10.899	10.923	11.107	10.936	10.956	11.029	10.92	10.674	10.915
sum	96.676	98.057	96.947	93.35	98.117	97.695	98.462	97.354	97.869	97.712	98.069	97.632	97.809	97.45	98.546	96.594	97.746

Si	6.8097159221	7.0088737536	6.9520964847	6.9045698838	6.9890836639	6.9944179148	6.950964533	7.0049302583	7.020723817	7.005802263	6.9566442172	7.0082576167	6.981803363	7.0305954952	7.029084603	6.9866414114	6.9950255704
Al	1.1902840779	0.9911262464	1.0479035153	1.0954301162	1.0109163361	1.0055820852	1.049035467	0.9950697417	0.979276183	0.994197737	1.0433557828	0.9917423833	1.018196637	0.9694045048	0.970915397	1.0133585886	1.0049744296
Al	3.3976680789	3.6349357243	3.6398255702	3.6200832395	3.5973619759	3.6817409255	3.6685939594	3.6565008786	3.6629765135	3.6721936806	3.6171160458	3.6497581821	3.6541647005	3.5921081327	3.6427673883	3.6239591324	3.6114354538
Fe(iii)	0	0	0	0	0	0	0	0	0	0	0	0	0	0	0	0	0

Ti	0.0216742662	0.0178104128	0.0325998411	0.0241317077	0.0270152261	0.023600835	0.0230785659	0.0264121777	0.0188141999	0.0235036123	0.0254412967	0.017240438	0.0240420142	0.0275211039	0.021999093	0.0255779609	0.0252560429
Cr	0	0	0	0	0	0.0030599377	0.0023825198	0	0.0008692754	0.0016324995	0.001418958	0.0010916747	0	0.0039447316	0.000540274	0	0
Fe(ii)	1.032932774	0.58297579	0.5978383121	0.659548553	0.571805567	0.5896144506	0.5444273051	0.5090148614	0.5234967997	0.5108664002	0.6190293667	0.562200549	0.5344640773	0.5751981527	0.5574989873	0.636370638	0.5784437892
Mn	0.004832812	0	0	0	0.0011655072	0	0.0029003318	0	0.0047724907	0.0017488272	0.0035078522	0.0011694646	0	0	0.0053247069	0	0.0100647816
Mg	0.4119605837	0.4037224581	0.3787693014	0.3809267408	0.435357959	0.323750693	0.3994502167	0.4247970528	0.4202551425	0.405945803	0.3916922308	0.4045160631	0.4116362295	0.4248328041	0.4065059561	0.3774254861	0.4161437849
Ca	0.0136023233	0	0.0008958523	0.0203749771	0	0	0.0001467543	0	0.0008834779	0.0010323735	0	0.0044380431	0.0011808722	0	0	0.001499304	0
Na	0.0937581895	0.0990229655	0.1242880591	0.1117384827	0.1920954486	0.0602976671	0.1107422481	0.1120374601	0.1028532811	0.121432975	0.1014445801	0.0993186017	0.1394343727	0.1211866961	0.110495232	0.103100251	0.1363619791
K	1.890167601	1.9426579605	1.9187324495	1.9052145421	1.9020159892	1.9697482013	1.939200302	1.9402571067	1.9108129137	1.9180849647	1.956082105	1.9262642197	1.925537748	1.9499128865	1.9038415054	1.9054782405	1.9239772059
TOTAL	14.8665966285	14.6811253113	14.6929493857	14.722018243	14.7268176729	14.6518127102	14.6909222031	14.6690195373	14.6457340945	14.656441136	14.7157324353	14.665997236	14.6904600144	14.6947045076	14.648973143	14.6734110129	14.7016830375

Glaucophane
Mica

	m8	m9	m10	m11	m12	m14	m15	m16	m17
SiO2	55.772	55.346	55.479	54.67	54.849	54.809	55.974	56.004	56.158
TiO2	0.074	0.013	0	0.094	0.064	0.094	0.064	0.028	0.003
Al2O3	10.208	10.321	10.226	10.704	10.352	10.674	10.36	10.574	10.379
Cr2O3	0.014	0	0	0	0	0	0	0	0
FeO	18.495	18.547	19.262	19.697	19.649	19.096	18.083	18.598	18.602
MnO	0.005	0	0.03	0.005	0	0	0.02	0	0

	m18	m19	m20	m21	m22	m23
SiO2	49.149	51.081	50.996	49.462	50.646	51.165
TiO2	0.236	0.266	0.189	0.264	0.238	0.193
Al2O3	28.806	28.897	24.053	28.711	27.772	27.983
Cr2O3	0	0.015	0	0.008	0	0.022
FeO	5.267	4.598	7.09	5.29	5.058	4.982
MnO	0.046	0.015	0	0	0.025	0.01

MgO	5.927	6.02	5.003	5.204	5.466	5.251	5.706	5.157	5.268
CaO	0.385	0.522	0.206	1.033	0.983	0.774	0.288	0.173	0.148
Na2O	7.36	7.284	7.189	6.771	6.858	7.089	7.349	7.175	7.252
K2O	0.021	0.027	0.016	0.069	0.052	0.073	0.025	0.02	0
sum	98.261	98.08	97.411	98.247	98.273	97.86	97.869	97.729	97.81

MgO	1.927	2.05	1.816	1.843	2.044	2.051
CaO	0	0.015	0.567	0.077	0	0.003
Na2O	0.615	0.348	3.384	0.542	0.407	0.397
K2O	10.669	10.55	8.779	9.748	10.907	11.032
	96.715	97.835	96.874	95.945	97.097	97.838

Si	7.8659103673	7.8204118988	7.9150510616	7.7598424136	7.7777912574	7.8079664424	7.9200684097	7.9372407531	7.95263221
Al	0.1340896327	0.1795881012	0.0849489384	0.2401575864	0.2222087426	0.1920335576	0.0799315903	0.0627592469	0.04736779
Al	1.5626043859	1.539092836	1.6343879371	1.5503658962	1.5077746158	1.5999885004	1.6476256165	1.7033595206	1.6847797052
Fe(iii)	0.4216808973	0.4794641437	0.396286086	0.4798411435	0.5073493574	0.3645324619	0.3109096586	0.3258524092	0.3260689681
Ti	0.0078497597	0.0013815882	0	0.0100351426	0.006825892	0.0100717696	0.0068110557	0.0029846981	0.0003195306
Cr	0.0015610101	0	0	0	0	0	0	0	0
Fe(ii)	1.7594928495	1.7119285663	1.901605985	1.8579572953	1.822517875	1.910206767	1.8286097138	1.8781897704	1.8766650398
Mn	0.0005972299	0	0.0036248087	0.0006010527	0	0	0.002396687	0	0
Mg	1.2462138676	1.2681328659	1.0640951832	1.1011994697	1.1555322598	1.1152005011	1.2036472683	1.0896136016	1.1121667563
Ca	0.0581721912	0.0790197791	0.031485764	0.157081872	0.1493354813	0.1181269361	0.0436573124	0.0262674872	0.0224534407
Na	2.0124214451	1.9953618933	1.9883916372	1.8632236556	1.885356132	1.9578498578	2.0159473451	1.9714272705	1.9909731742

Si	6.5810898767	6.7031518071	6.8860088381	6.6318994881	6.7364058439	6.7503087295
Ti	0.0237617424	0.0262472885	0.0191900635	0.0266166463	0.0238036302	0.0191465756
Al	4.5465438356	4.4697961039	3.8283885178	4.5376382699	4.3541715948	4.3517127491
Fe	0.5897250907	0.504535562	0.800535969	0.5930961241	0.5625551046	0.549613678
Mn	0.005216506	0.001667054	0	0	0.0028161893	0.0011173504
Mg	0.3845758215	0.4009504001	0.3654806876	0.3683059402	0.405210892	0.4033048491
Ca	0	0.0021087876	0.0820231495	0.0110606056	0	0.0004240273
Na	0.1596439944	0.0885305663	0.8858417639	0.1408834191	0.1049474369	0.1015396117
K	1.8222831857	1.7659611322	1.5121174639	1.6672118934	1.8505355104	1.8565811109
Sum	14.1128400531	13.9629487017	14.3795864534	13.9767123869	14.0404462021	14.0337486817

K	0.0037779925	0.0048664938	0.0029117501	0.0124928618	0.0094058907	0.0132653263	0.004512234	0.0036156761	0
TOTAL	15.0743716288	15.0792481661	15.0227891513	15.0327983894	15.0440975041	15.0892421201	15.0641168915	15.0013104337	15.0134266149

Sy2_omp_line

	1	2	3	4	5	6	7	8	9	10	11	12	13	14	15	16	17	18	19	20	21	22	23
SiO2	55.266	55.555	55.539	55.373	55.411	55.623	55.459	55.499	55.582	56.002	55.375	55.668	54.98	56.036	56.282	55.534	56.123	56.057	56.229	55.698	51.314	56.004	55.756
TiO2	0.137	0.028	0.049	0.062	0.028	0.046	0	0.018	0	0.049	0.072	0.044	0.005	0.057	0.008	0.008	0.026	0.008	0	0.005	0.026	0.036	0
Al2O3	11.252	13.53	13.484	12.786	12.168	13.179	13.521	13.997	13.742	13.852	12.662	13.635	11.231	12.84	14.345	12.55	13.403	13.471	12.782	12.443	30.507	14.237	13.537
FeO	15.286	13.653	13.685	14.159	14.915	14.209	14.143	13.295	13.493	12.849	14.412	13.516	15.072	14.138	12.93	14.474	13.913	13.988	14.668	14.51	6.147	13.229	13.809
MnO	0.065	0.181	0.055	0.086	0.075	0.065	0.101	0.096	0.116	0.02	0.101	0.04	0	0.01	0.03	0.065	0.045	0.156	0.131	0.106	0.025	0.06	0.126
MgO	1.734	0.942	1.27	1.246	1.162	1.07	0.899	1.109	0.979	1.111	1.259	1.041	1.4	1.273	1.103	1.301	1.031	1.093	1.087	1.399	0.416	0.854	0.989
CaO	3.893	2.309	3.12	2.978	3.011	2.662	2.356	2.652	2.415	2.713	2.974	2.596	3.479	2.789	2.314	3.151	2.619	2.498	2.66	3.335	1.032	2.349	2.292
Na2O	11.879	12.942	12.688	12.706	12.12	12.824	12.8	12.558	12.723	12.62	12.463	12.686	11.837	13.007	13.11	12.138	12.538	12.753	12.57	12.912	9.098	13.022	13.015
K2O	0.033	0.019	0.013	0.024	0.028	0.028	0.025	0	0.004	0.024	0.016	0.024	0	0.02	0.012	0	0.011	0.003	0.011	0.011	0.898	0.003	0
Cr2O3	0.04	0	0	0.024	0	0	0	0	0	0	0	0.043	0.006	0	0	0.034	0	0	0.003	0.018	0.021	0	0
sum	99.585	99.159	99.903	99.444	98.918	99.706	99.304	99.224	99.054	99.24	99.334	99.293	98.01	100.17	100.134	99.255	99.709	100.027	100.141	100.437	99.484	99.794	99.524

Si	2.0493208937	2.04397989	2.0316064179	2.0412011327	2.0568658491	2.0418558396	2.0411437123	2.0349397453	2.0431597532	2.0470944294	2.0441629361	2.0423414166	2.0653295241	2.0476444439	2.039017229	2.0498761345	2.0513088289	2.0453584555	2.0559216956	2.0398590719	1.7806047184	2.0394632811	2.044272313
Ti	0.00381	0.00077	0.00134	0.00171	0.00078	0.00126	0	0.00049	0	0.00134	0.001998561	0.00121	0.0001412335	0.00156	0.00021	0.00022	0.00071	0.00021	0	0.00013	0.00067	0.00098	0

	99321	46306	77854	85516	15399	97308		62746		68324		38319		61935	79338	20454	45731	9489		76936	84036	57856	
Al	0.4918095403	0.5867681791	0.5814007056	0.5555686586	0.5324078755	0.5702540998	0.5865778404	0.6049460556	0.5954336711	0.5968457594	0.5509591119	0.5896484464	0.4972998583	0.553054251	0.6125862107	0.5460440505	0.5774408174	0.5793682679	0.5508841959	0.5371566479	1.2478041983	0.6111258005	0.5850390519
Fe	0.4739679135	0.4200342537	0.418590602	0.4364389282	0.4629524521	0.4361514631	0.4352574787	0.4076222572	0.4147437281	0.3927415229	0.4448659594	0.4146427351	0.4734331399	0.4319948302	0.3916995296	0.4467457021	0.4252204161	0.4267743934	0.4484564374	0.4443560805	0.1783602263	0.4028348282	0.4233626281
Mn	0.0020412868	0.0056398919	0.0017038955	0.0026848804	0.0023578164	0.0020207974	0.0031481953	0.0029810988	0.0036113109	0.0006191603	0.0031576347	0.0012428578	0	0.0003094754	0.0009204737	0.0020319862	0.0013929689	0.0048206202	0.0040565445	0.0032877983	0.0007347006	0.0018504904	0.0039125187
Mg	0.0958336775	0.0516560859	0.0692408462	0.0684577964	0.0642884912	0.0585425414	0.0493149238	0.0606059228	0.0536374315	0.0605292822	0.0692699105	0.0569233671	0.0783844255	0.0693318758	0.0595585357	0.071575285	0.0561650258	0.0594397352	0.0592369759	0.0763651842	0.0215150375	0.0463523589	0.0540456264
Ca	0.1546529676	0.0910121384	0.122269471	0.1176073217	0.1197409375	0.1046889004	0.0928963722	0.1041745984	0.0951058452	0.1062444009	0.1176155256	0.1020350386	0.1400106158	0.1091837117	0.0898124714	0.1246060088	0.1025528157	0.0976458818	0.1041956925	0.1308513841	0.038364829	0.0916435237	0.0900292578
Na	0.8539376294	0.9231009462	0.8997648522	0.9080106288	0.8721816262	0.9126169091	0.9132840073	0.8926499994	0.9066757838	0.8943098788	0.8919052069	0.902280906	0.8620264654	0.9214226738	0.9207641449	0.8685806108	0.8884086348	0.90208253	0.8909961374	0.9167447146	0.6120288809	0.9193245729	0.9250935303
K	0.0015608993	0.0008916945	0.0006065881	0.0011285167	0.001325797	0.0013111057	0.0011736824	0	0.0001875587	0.0011190632	0.0007534089	0.0011231635	0	0.0009322372	0.0005545512	0	0.0005128518	0.0001396271	0.0005130361	0.0005138807	0.0397481576	0.0001393565	0
Cr	0.0011726187	0	0	0.0006994294	0	0	0	0	0	0	0	0.0012472	0.000178189	0	0	0.0009921846	0	0	8.67186221847847E-005	0.0005211683	0.0005760973	0	0
Sum	4.12694	4.12385	4.12653	4.13281	4.11290	4.12871	4.12279	4.10841	4.11255	4.10085	4.1246882549	4.11145	4.1166252624	4.13543	4.11513	4.10968	4.10371	4.11584	4.1142607152	4.14927	3.91983	4.11371	4.1257549262

	47403	77102	1164	64151	23848	13871	62123	5952	50825	03295		17631		96925	10799	18233	69325	90001		24558	91522	99977	

	24	25	26	27	28	29	30	31	32	33	34	35	36	37	38	39	40	41	42	43	44	45	46
SiO2	56.133	56.615	56.251	55.694	56.033	56.019	54.131	55.565	56.791	56.317	56.111	56.08	55.836	56.76	57.348	56.084	55.786	53.288	56.57	54.877	55.887	55.79	55.633
TiO2	0.026	0.031	0.021	0.041	0.114	0.065	0.07	0	0.01	0.023	0.096	0.052	0.021	0	0.052	0.028	0.01	0.116	0.067	0.064	0.028	0.07	0.07
Al2O3	13.621	15.063	14.075	14.599	13.359	12.236	10.902	11.288	15.012	13.706	13.479	13.586	12.104	16.74	15.223	12.916	14.289	12.238	11.307	10.723	13.544	13.868	12.649
FeO	13.82	12.894	13.277	13.559	13.999	14.663	16.17	15.255	12.285	13.802	13.932	13.956	14.55	11.045	11.391	13.782	12.804	15.429	15.303	15.877	13.621	13.191	14.507
MnO	0.156	0.101	0.081	0.116	0.045	0.035	0.126	0.075	0.106	0.076	0.151	0.035	0	0	0.04	0.02	0	0.231	0.106	0.086	0.086	0.096	0.045
MgO	1.039	0.833	0.898	1.108	1.097	1.377	1.804	1.636	0.779	0.869	1.085	1.054	1.328	0.504	0.814	0.998	0.881	1.728	1.629	1.682	1.079	1.014	1.092
CaO	2.409	1.914	2.255	2.764	2.747	3.426	4.448	3.74	1.621	2.203	2.707	2.419	3.176	1.236	1.656	2.259	2.309	6.017	3.744	4.127	2.485	2.589	2.575
Na2O	13.22	13.219	12.837	12.72	12.585	12.115	11.062	12.043	13.461	12.908	13.03	12.898	12.42	13.982	13.228	12.572	12.729	10.295	12.062	11.799	12.821	12.535	12.328
K2O	0.009	0.01	0.013	0.05	0	0.003	0.018	0.009	0.003	0.016	0	0	0.002	0.024	0.012	0.005	0.018	0.005	0.01	0.005	0.01	0.018	0.02
Cr2O3	0.01	0	0.04	0.024	0.032	0	0	0.021	0.016	0.003	0.003	0	0	0	0	0.01	0.031	0.022	0.013	0.006	0	0	0.002
sum	100.443	100.68	99.748	100.675	100.011	99.939	98.731	99.632	100.084	99.923	100.594	100.08	99.437	100.291	99.764	98.674	98.857	99.369	100.811	99.246	99.561	99.171	98.921

Si	2.0407310077	2.0354293866	2.047435454	2.0166708407	2.0448000173	2.0553821174	2.0367995366	2.0572382569	2.0469090128	2.0517636444	2.0388289316	2.0439337121	2.0591891476	2.0271760158	2.0595941369	2.0682865917	2.0443000021	1.9918807489	2.0662169132	2.0510411656	2.0455174263	2.0440450511	2.0572345303
T	0.0	0.0	0.0	0.0	0.0	0.0	0.0	0	0.0	0.0	0.00	0.0	0.00	0	0.0	0.0	0.0	0.0	0.00	0.0	0.0	0.0	0.00

i	007107617	008380489	005747545	011163326	031282032	017933032	019805391		002710205	006300845	26229328	014250998	05823504		014042675	00776449	002755514	032604313	18401265	01798652	007706081	019284807	19464019
Al	0.5837028223	0.638338877	0.6038702937	0.6231104107	0.5746404655	0.5291904285	0.4835303128	0.4926239979	0.6377828963	0.5885912969	0.5773055634	0.5836677569	0.5261700785	0.7047252244	0.6444346864	0.5614551407	0.6172150869	0.5392121293	0.4868020697	0.4724062252	0.5843252073	0.5989122905	0.5513441976
Fe	0.4201251731	0.3876281836	0.4040946295	0.4105418364	0.4271762806	0.4498660379	0.5087628702	0.472279002	0.3702519331	0.4204680424	0.4233010993	0.4253269621	0.4486917528	0.3298511057	0.3420805436	0.4249982414	0.3923450914	0.4822528958	0.4673792886	0.4961986883	0.4168737325	0.404124308	0.4485719243
Mn	0.004803202	0.0030752798	0.0024969148	0.0035573233	0.0013907793	0.001087587	0.0040152401	0.0023517074	0.0032356656	0.0023449854	0.004646741	0.0010803528	0	0	0.00121664	0.0006246554	0	0.0073128158	0.0032789466	0.0027222074	0.0026658124	0.0029788187	0.0014092972
Mg	0.0562989355	0.0446361426	0.0487162033	0.0597975643	0.0596665213	0.0753023081	0.1011709659	0.0902783678	0.0418478939	0.0471872557	0.0587597099	0.0572554113	0.0729956774	0.0268285212	0.0435717398	0.0548554021	0.0481185399	0.0962708436	0.0886804613	0.0936973122	0.0588614501	0.055371869	0.0601853915
Ca	0.093826654	0.0737205185	0.0879323009	0.1072226573	0.1073958608	0.1346686478	0.1793035693	0.1483463259	0.062592739	0.0859853047	0.105376302	0.0944531811	0.1254828445	0.047292194	0.0637155772	0.0892503414	0.0906494678	0.2409549453	0.1465033287	0.1652495949	0.097440768	0.1016220781	0.1020118158
Na	0.9317369077	0.9213347786	0.9058115353	0.8929107542	0.8903371988	0.8617374638	0.8069195273	0.8643950946	0.9405690426	0.911677232	0.9178496121	0.9113296673	0.8879691383	0.9680832463	0.9209835867	0.8988152703	0.9042906221	0.7460270909	0.8540895172	0.8549162077	0.9097218387	0.8903336225	0.883768026
K	0.0004173679	0.0004585995	0.0006035765	0.0023094344	0	0.0001404066	0.0008639404	0.0004250449	0.000137927	0.0007435614	0	0	9.4085124953297E-005	0.0010933755	0.0005497353	0.0002352073	0.0008413969	0.0002384037	0.0004659065	0.0002383763	0.0004668758	0.0008412317	0.000943388
Cr	0.000287417	0	0.0011510253	0.0006870412	0.0009232129	0	0	0.0006146777	0.000455915	0.000086408	8.6178501552377E-005	0	0	0	0	0.0002915524	0.0008981027	0.0006501319	0.0003753859	0.0001772883	0	0	5.8469075342284E-005
S	4.1	4.1	4.1	4.1	4.1	4.1	4.1	4.1	4.1	4.1	4.12	4.1	4.12	4.1	4.0	4.0	4.0	4.1	4.11	4.1	4.1	4.1	4.10

um	323528318	054598151	015356626	172371539	085353269	091683003	233465017	279377973	035981307	093914073	86908922	184721433	11750745	050496829	775509134	992972992	980357585	074103046	52565584	382684294	166437192	001577501	74149724

Table 3: Microprobe data of clinozoisite and omphacite in eclogite sample SY4. See Fig. 3D for location of measurements.

epidote-clinozoisite

	sy4_m1	sy4_m2	sy4_m3
SiO2	38.537	38.171	38.518
TiO2	0.116	0.108	0.089
Al2O3	25.372	25.529	25.606
FeO	10.695	10.225	10.083
MnO	0.172	0.107	0.07
MgO	0.066	0.042	0.049
CaO	23.176	23.152	23.265
Na2O	0.04	0.024	0
K2O	0	0	0.008
Cr2O3	0.048	0.046	0.058
sum	98.222	97.404	97.746
Si	3.08	3.07	3.09
Ti	0.01	0.01	0.01
Al	2.39	2.42	2.42
Fe	0.72	0.69	0.68
Mn	0.01	0.01	0.00
Mg	0.01	0.01	0.01
Ca	1.99	2.00	2.00
Na	0.01	0.00	0.00
K	0.00	0.00	0.00
Cr	0.00	0.00	0.00
Sum	8.21	8.21	8.19

omphacite

	sy4_m4	sy4_m5	sy4_m6	sy4_m7	sy4_m8	sy4_m9	sy4_m10
SiO2	55.937	55.711	55.136	55.123	55.761	55.102	57.561
TiO2	0.048	0.066	0.019	0.056	0.045	0.055	0.053
Al2O3	11.561	10.26	9.066	10.244	11.069	10.942	9.64
FeO	9.513	11.29	12.273	10.74	9.554	10.259	13.106
MnO	0.011	0.091	0.155	0.166	0.021	0.059	0.112
MgO	4.821	4.642	4.927	4.98	5.159	5.159	9.377
CaO	7.892	8.314	8.648	9.513	8.743	9.167	0.256
Na2O	9.724	9.568	9.188	8.652	9.4	9.184	7.663
K2O	0.019	0.013	0	0	0	0	0.002
Cr2O3	0.039	0.057	0.023	0.052	0.011	0.056	0.006
sum	99.565	100.012	99.435	99.526	99.763	99.983	97.776
Si	2.03	2.03	2.04	2.02	2.02	2.01	2.09
Ti	0.00	0.00	0.00	0.00	0.00	0.00	0.00
Al	0.49	0.44	0.40	0.44	0.47	0.47	0.41
Fe	0.29	0.34	0.38	0.33	0.29	0.31	0.40
Mn	0.00	0.00	0.00	0.01	0.00	0.00	0.00
Mg	0.26	0.25	0.27	0.27	0.28	0.28	0.51
Ca	0.31	0.33	0.34	0.37	0.34	0.36	0.01
Na	0.68	0.68	0.66	0.62	0.66	0.65	0.54
K	0.00	0.00	0.00	0.00	0.00	0.00	0.00
Cr	0.00	0.00	0.00	0.00	0.00	0.00	0.00
Sum	4.06	4.08	4.09	4.06	4.07	4.08	3.97

Table 4: P- and S-wave velocities and anisotropies of samples SY1, SY2, SY4 and SY5. Iso is the VRH isotropic average.

Sample	Lithology	**Vpiso (km/s)**	min (km/s)	max (km/s)	Ap (%)	**Vsiso (km/s)**	Vs1 min (km/s)	Vs1 max (km/s)	Vs2 min (km/s)	Vs2 max (km/s)	**Vp/Vs**
Sy1	Blueschist	7.82	7.15	8.09	12.1	4.45	4.40	4.73	4.40	4.51	1.76
Sy2	Eclogite	7.89	7.76	8.06	3.7	4.64	4.62	4.70	4.60	4.64	1.70
Sy4	Eclogite	7.76	7.64	7.90	3.3	4.58	4.55	4.64	4.54	4.59	1.69
Sy5	Blueschist	7.43	7.24	7.72	6.5	4.35	4.34	4.43	4.28	4.37	1.71

Table 5: Tensor components of elastic moduli for the four samples studied.

	SY1	SY2	SY4	SY5
C11C11	65.1	64.7	61.2	59.5
C12C12	17.1	20.0	17.7	17.2
C13C13	20.5	19.5	18.7	17.9
C14C14	0.5	0.1	0.1	-0.2
C15C15	-0.1	-0.2	0.6	-0.4
C16C16	0.1	0.3	0.4	0.1
C22C22	51.3	63.3	58.5	52.6
C23C23	17.0	19.4	17.8	17.0
C24C24	0.7	0.3	-0.1	-0.4
C25C25	0.0	-0.1	-0.2	0.0
C26C26	0.0	0.2	0.1	0.1
C33C33	64.9	60.4	60.8	54.6
C34C34	1.3	0.3	-0.1	-0.4
C35C35	-0.1	-0.2	0.5	-0.2
C36C36	0.0	0.0	0.1	0.0
C44	19.5	21.2	20.7	18.4
C45	0.0	0.1	0.1	0.0
C46	0.0	-0.1	0.0	-0.1
C55	22.3	21.4	21.5	19.3
C56	0.4	0.1	0.1	-0.2
C66	19.4	22.0	20.7	18.9

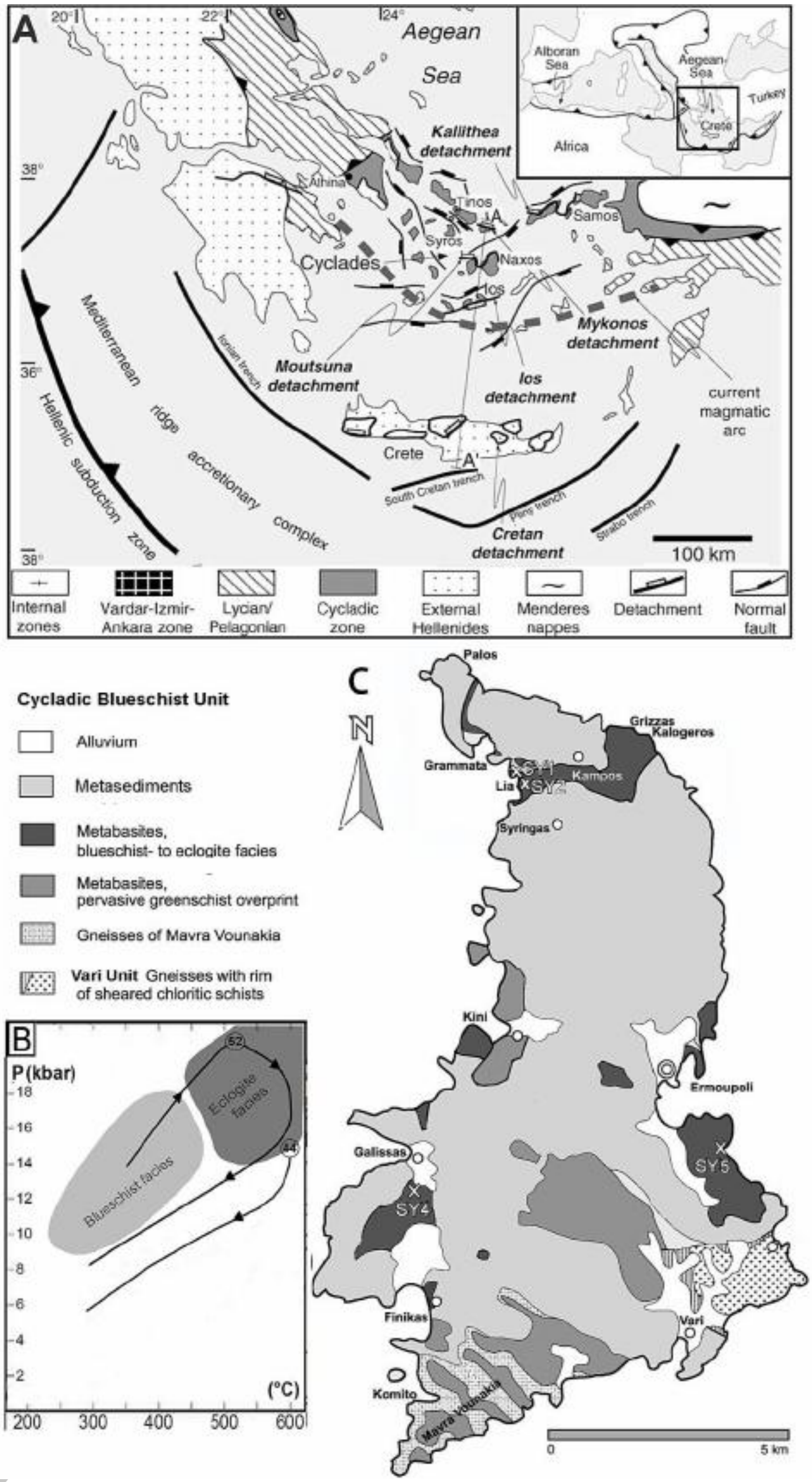

Fig. 1: A: Overview map of the Cyclades (after Ring et al., 2003); B: Pressure-Temperature path of Syros (upper path) and Sifnos (lower path) from Jolivet and Brun (2010) based on the data from Trotet et al. (2001a; b), numbers indicate time of peak pressure metamorphism in Ma; C: Map of the major lithological units of Syros (from Keiter et al., 2004).

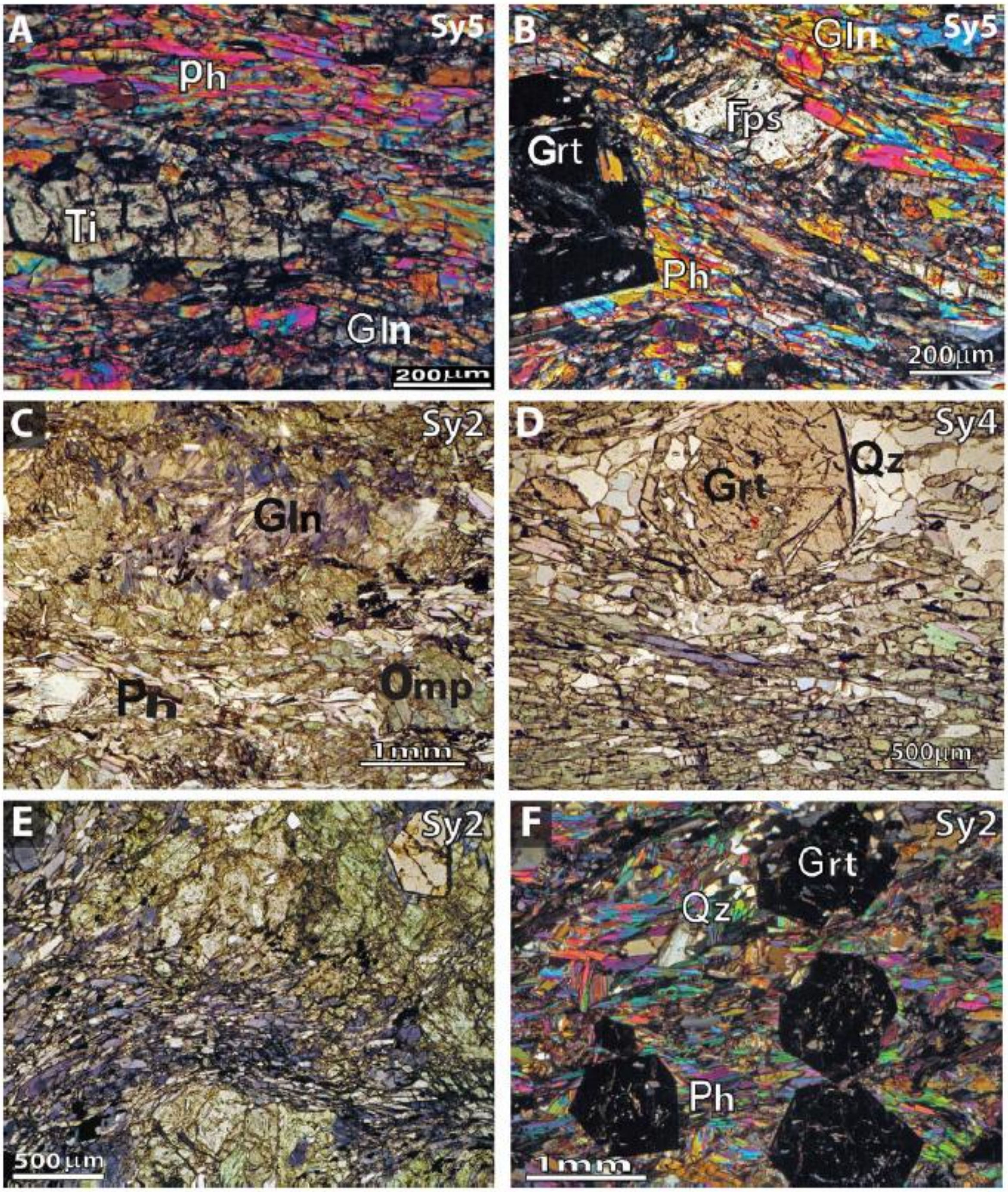

Fig. 2: Light-optical micrographs of the investigated blueschist (A, B) and eclogite (C-F) samples. (A) Well aligned Ph: phengite, Ti: titanite and Gln: glaucophane in the foliation of a blueschist; (B) phengite and glaucophane in pressure shadows of feldspar and garnet; (C) coarse-grained eclogite with randomly oriented amp: amphibole, phengite and omphacite; (D) quartz in pressure shadows of garnet, surrounded by a matrix of omphacite and glaucophane, well aligned in the foliation; (E) coarse and randomly oriented omphacite grains divided by a zone of small glaucophane grains well aligned in a microshear zone; (F) randomly aligned quartz and phengite in pressure shadows of garnet. Sections are perpendicular to the foliation and parallel to the lineation. A, B, F taken under crossed polarizers, C, D, E under plane-polarized light; Fps: feldspar, Gln: glaucophane, Grt: garnet, Omp: omphacite, Ph: phengite, Qz: quartz, Ti: titanite. All micrographs are taken from sections parallel to the lineation and perpendicular to the foliation.

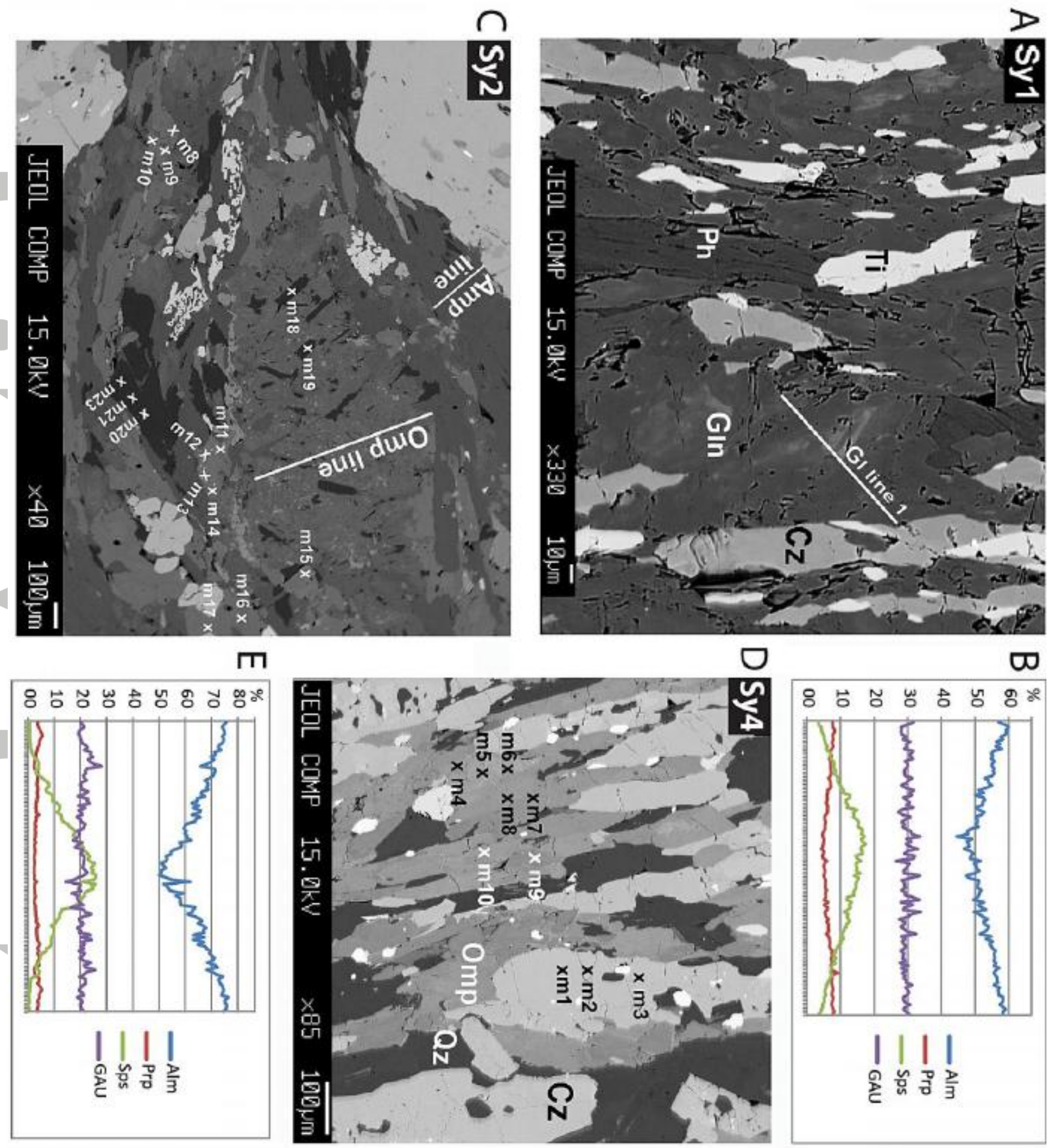

Fig. 3: A; C and D: Backscatter electron (BSE) images of blueschist (A) and eclogites (C and D); Amp: amphibole, Cz: clinozoisite, Gln: glaucophane, Omp: omphacite, Ph: phengite, Qz: quartz, Ti: titanite. Sample numbers are given in the upper left of each image. (m1-m23): icroprobe measurement points and measurement profiles (Table 2A, B). B and E: Volume % of garnet components in blueschist sample SY1 (B) and eclogite sample SY2 (E); Alm: almandine, Prp: pyrope, Sps: spessartine, GAU: Grossular+Andradite+Uwanovite. All BSE images are taken from sections parallel to the lineation and perpendicular to the foliation.

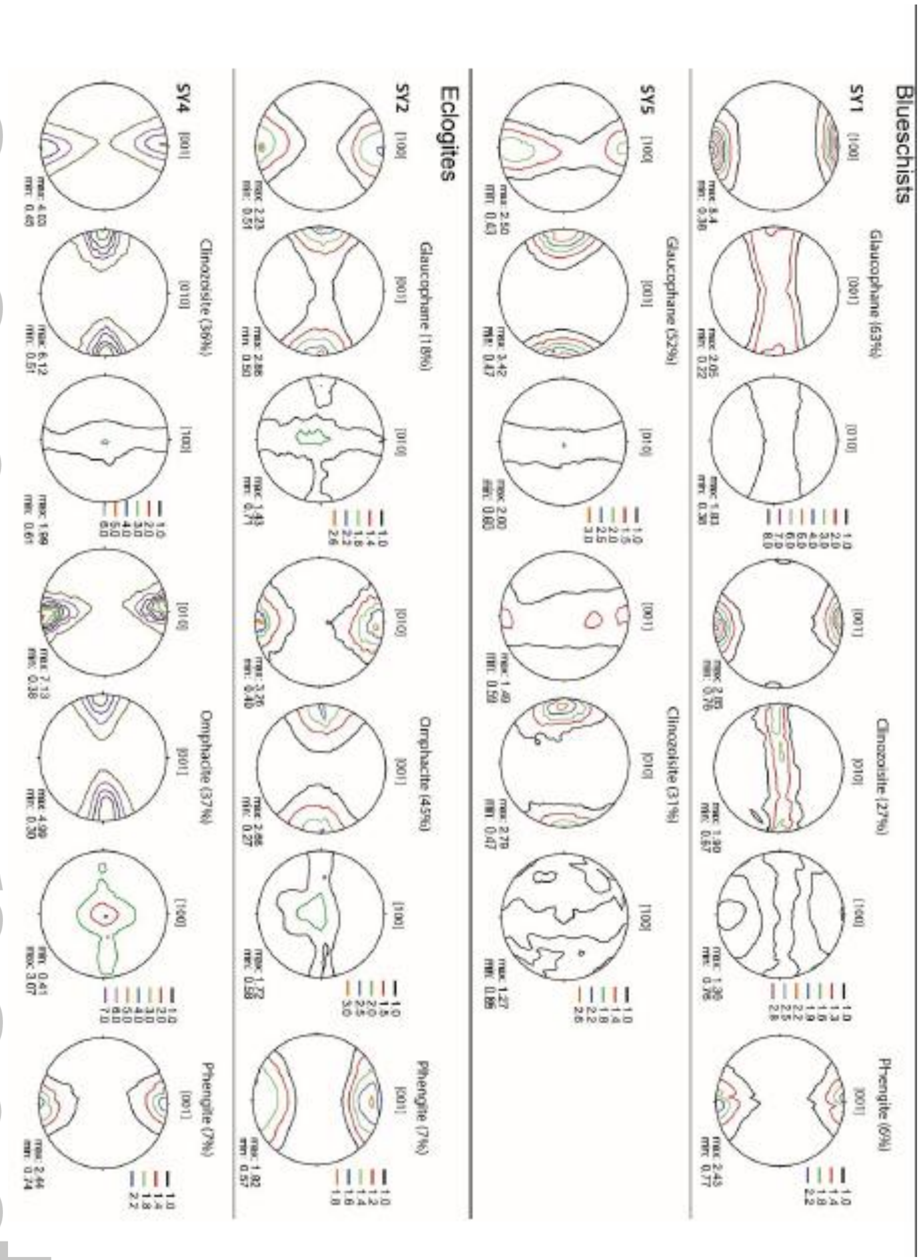

Fig. 4: CPO data of the mineral phases that are important for the elastic anisotropy of the blueschist (SY1, SY5) and eclogite (SY2, SY4) samples. Pole figures are oriented according to foliation and mineral/stretching lineation of glaucophane and omphacite, respectively. The lineation (X-direction of the finite strain ellipsoid) is EW in the pole figure, the foliation normal (Z-direction of the finite strain ellipsoid) is oriented NS, and the Y-direction (perpendicular to X and Z) lies normal to the pole figure plane. Pole figures are lower hemisphere equal area projections on a 5x5° grid. Contour levels are multiples of a random distribution. Maxima are indicated at the lower right of each pole figure. Only significant pole figures are given. They illustrate the textural differences between samples. See text for pole figure description and discussion.

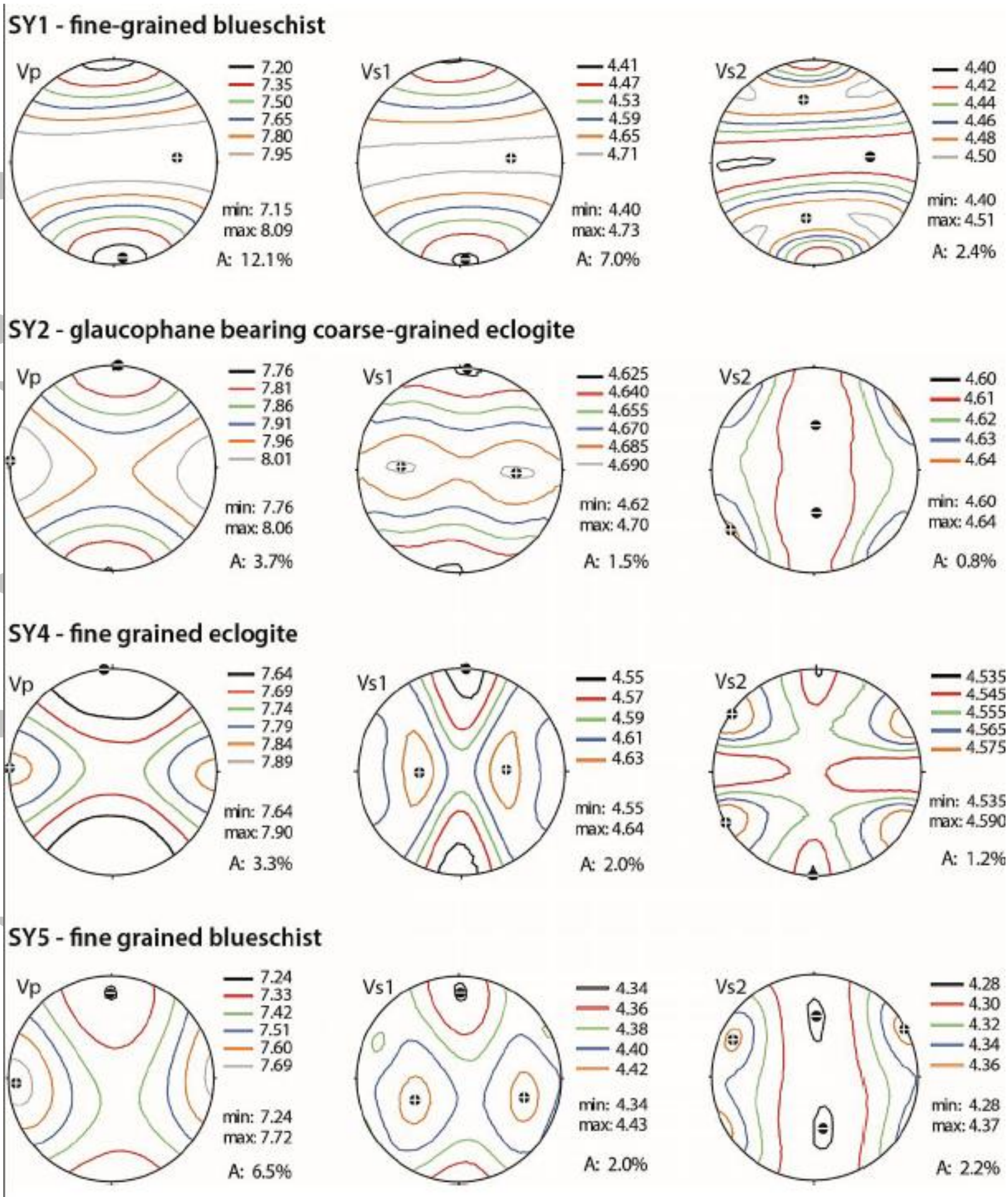

Fig. 5: Modelled P-wave and S-wave velocity distributions of the two blueschist (SY1, SY5) and the two eclogite (SY2, SY4) samples. Colored contour lines show velocities in km/s. Minimum and maximum velocity is given in the lower right corner of the pole figures, and orientation zones of maximum velocity are surrounded by grey or orange contour lines. A: elastic anisotropy. See text for discussion.